ELSEVIER

Physica D 88 (1995) 55–81

PHYSICA D

A paraxial model for optical self-focussing in a nematic liquid crystal

David W. McLaughlin [a], David J. Muraki [a], Michael J. Shelley [a], Xiao Wang [b]

[a] *Courant Institute of Mathematical Sciences, New York University, 251 Mercer Street, New York, NY 10012, USA*

[b] *Department of Mathematics, The Hong Kong University of Science and Technology, Clear Water Bay, Kowloon, Hong Kong, China*

Received 19 October 1994; revised 17 April 1995; accepted 17 April 1995

Communicated by H. Flaschka

Abstract

Numerical and asymptotic results are presented for a coupled PDE system that models recent experiments of the self-focussing of laser light in a nematic liquid crystal. This study complements previous asymptotic analyses which, in a narrow-beam limit, describe two essential features observed in nematic self-focussing – the *undulation* and *filamentation* of a laser beam. These numerical computations represent a direct emulation of the experimental configuration within the context of a paraxial PDE model. In addition to providing numerical corroboration to these earlier asymptotic analyses, these results suggest that initial focussing caustics play a critical rôle in the formation of beam filament pairs.

1. Introduction

Typical self-focussing experiments require high-intensity pulsed lasers ($\sim$ MW/cm^2) for weak nonlinear effects to become apparent [1]. By comparison, the optical nonlinearity of a nematic liquid crystal is enormous – a factor of 6–10 orders of magnitude larger than doped glasses is not uncommon [2]. As a result, strong self-focussing of light can be achieved in a nematic crystal using continuous-wave lasers of moderate power ($\sim$ kW/cm^2) in a much less exotic experimental setting. In nematics, most previous works study the focussing by thin-films [3] where the focussing occurs external to the media. Recent experiments of Braun et al. [4] in long nematic samples observed an unexpected sequence of complex optical beam structures where the self-focussing occurred within the media itself. Most notably, as optical intensity was increased, these experiments demonstrated first, the formation of focal spots, followed by an off-axis meandering (undulation) and a break-up (filamentation) of the beam (Fig. 1) [5]. The numerical computations presented here were designed to mimic this experimental configuration up to the simplifications inherent in a paraxial PDE model.

In our numerical emulation of the original experiments, it was also possible to follow the development of spatial structure with increasing input beam intensity. These computations successfully recovered the most salient features of the experimental observations; and in this sense form, together with the physical experiments and concurrent asymptotic analyses, a comprehensive investigation of these optical self-focussing phenomena. The major result of these computations is a possible mechanism for beam filamentation, in which *filament pairs originate from caustics created*

Elsevier Science B.V.
SSDI 0167-2789(95)00187-5

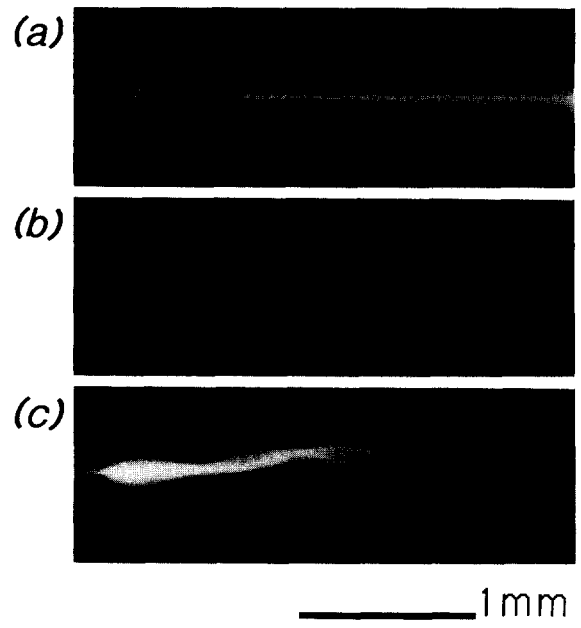

Fig. 1. Three longitudinal photographs of the self-focussing process in a capillary tube from ([5]). Images (a)–(c) show the development of optical structure – focal spot, undulation, filamentation – as the input beam intensity is increased.

by extreme focussing at the first focal spot.

Several reduced mathematical models for the optical self-focussing process in a bulk of nematic liquid crystal have been derived beginning from the most fundamental coupled field models for light and nematics – the vector forms of the Maxwell and Frank free-energy equations [6]. One particularly simple model PDE captures the essential coupling between optical refraction and nematic deformation, and evinces two of the most intriguing of the experimentally-observed features, *undulation* and *filamentation* [5]. The analysis is based upon our development of a matched-asymptotic adaptation of geometrical optics [7,8]. This *optical free-boundary* analysis exploits a separation of scales induced by the high-wavenumber nature of light to obtain two decoupled systems, distinguished by spatial scale, each of which provides a theoretical corroboration of these unusual nonlinear optical behaviors.

At the heart of this derivation, however, lies the assumption that the light energy remains confined by self-focussing into a narrow beamline region – and that the required separation of spatial scales is somehow initiated naturally through the self-focussing process. Since the asymptotic analysis essentially assumes quasi-steady propagation, it neglects any effects of the finite extent of the medium – the question of what initial scales are realized with the actual experimental set-up is beyond the scope of this approach. One of the primary aims of these computations then, is to establish to what degree this creation of scales, and its associated optical structures, might be an inevitable consequence of the initial self-focussing at the first focal spot.

The *paraxial PDE model* used in this study models the interaction between optics and nematic by the propagation of a parabolic wave through a nonlinear Poisson-type medium. Although much simplification is obtained by considering only a two-dimensional spatial $(x\text{–}z)$ domain, the need to resolve structure over a wide range of spatial scales poses considerable computational difficulty. In particular, the high-wavenumber character of optics in the parabolic wave equation produces extremely rapid transverse (x) oscillations across very narrow beams. On the other hand, the elliptic nature of the nematic equation supports structure over the full computational domain. For the most effective resolution, a non-uniform gridspacing is utilized for the transverse (x) coordinate whenever possible – this concentrates the numerical effort at the center of the paraxial beam. Stability considerations for the parabolic wave dictates a finer longitudinal (z) grid, and requires additional interpolation of the Poisson field.

This paper begins with abbreviated overviews of the original experiments, the PDE modelling and the optical free-boundary asymptotic theory. Next, the numerical method and implementation are presented. This is followed by the computational results – these are roughly organized into two sequences. The first mimics the experiments by showing the development of beam structure with increasing input intensity. The second benchmarks the generation of spatial structure in the approach to the high-wavenumber limit. Lastly, an asymptotic construction of two types of waveguide structures produces a scaling argument in support of a connection between the numerically-produced caus-

tics with the birth of the asymptotically-predicted filaments.

2. Experiments & theory

The initial motivation for studying the optics of nematic liquid crystals was to investigate the possibility of complex spatio-temporal behaviors in a strongly nonlinear system. Although the (non-thermal) optical response of nematic materials is typically too slow for direct feedback with light, the nonlinear self-focussing proved sufficiently powerful to induce an unusual cascade of time-independent spatial structures. While the details of these experiments and the resulting mathematical theory is presented elsewhere [4,8], brief overviews of these follow.

2.1. Optics in a tube

As a medium for a nonlinear optical experiment, the dominant attributes of nematic liquid crystals are its extremely strong nonlinear response and its strict anchoring conditions at boundaries. Although the self-focussing of light by thin films of nematic is a well-documented phenomena [3,9], these most recent experiments were designed specifically to investigate the self-focussing process in a thick nematic media, where the focussing occurs within the nonlinear medium itself. The most successful configuration for these studies involved the directing of a continuous wave (CW) beam of linearly-polarized laser light along the axis of a nematic-filled capillary tube.

The unique aspect of this choice of geometry was that a microscope could be used to visualize the longitudinal propagation of the beam. Unlike most experiments where only near- or far-field projections are obtainable, the small diameter of the capillary tube permitted a clear longitudinal view of transverse structures developing in the beam as it propagated through the medium. The experimental photographs (Fig. 1) clearly show that the beam develops unusual spatial structure – time-independent features which become increasingly-complex with higher intensities of the incoming light.

A characteristic feature of nematic optics is the *Frederiks transition*, an intensity threshold that is required in order to establish optical self-focussing. Beyond this transition three basic stages in the development of optical structure were identified:

- **a**: formation of focal spots (distinctive narrowing of the beam),
- **b**: undulation (off-axis wandering of the beam),
- **c**: filamentation (break-up into a multiple-beam structure).

These basic features are illustrated by the photographs in Fig. 1. The first image **a** shows the intense (transverse) focussing into a narrow beam which follows the tube axis – in fact, the formation of a single focal spot can be seen in the figure. The second image **b** captures, at a higher input laser intensity, the development of undulations – off-axis wandering of the beam in a manner that could be interpreted as oscillatory. And the final image **c** shows, at the highest beam intensities, the rather striking break-up of the beam into two distinct co-propagating filaments.

The photographs in Fig. 1 represent a distinguished plane of optical interest defined by the tube axis and the linear polarization of the incoming beam. The planar character of these optical structures is easily verified by a 90° rotation of the cross-sectional view where neither undulation, nor filamentation is discerned. As a final note, it is emphasized that all of these observations are made after the relaxation of initial transients and are therefore *time-independent* phenomena.

2.2. Optical free-boundary asymptotics

As an applied mathematical problem, the distinguishing character of this light-nematic system derives from the wide variation of active spatial scales involved. The short scale ($\lambda \approx 0.5\ \mu$m) is set by the optical wavelength for blue-green laser light. The large scale ($r_c \approx 0.75$ mm) is introduced through the nematic geometry and defined to be the capillary tube radius. In the non-dimensionalized governing equations for this light/nematic system, this separation of scales appears as a large dimensionless wavenumber parameter

$$k = \frac{2\pi r_c n_{\|}}{\lambda} \approx 1.4 \times 10^4 \qquad (1)$$

where $n_{\|} \approx 1.5$ is the minimum index of refraction for the nematic liquid crystal.

The rationale behind the optical free-boundary methodology derives from the observation that, in the experiments, the laser light is strongly confined into a relatively narrow beam near the capillary axis. This seemed to suggest the possibility of a *self-focussed nematic waveguide*, where the nematic deformation creates a refractive index profile that confines the propagation of light to a narrow beamline. Thus, the Maxwell equation need only be solved within a narrow beamline whose k-dependent width is determined by a matched asymptotic balance between diffraction and nematic refraction. On the other hand, the nematic equation is solved on the full domain and is free of the electric field coupling everywhere except in the vicinity of the beamline region.

One perspective on this optical free-boundary methodology is that the two fields are scale-separated through an interior-layer type of asymptotics, which is then wedded to a large-wavenumber (k) paraxial theory that describes the optical beam propagation. In this manner, the coupled PDE model decomposes into:

- an outer free-boundary problem for the nematic orientation field; and
- an inner paraxial wave evolution for the optical intensity field.

But most surprisingly, these problems truly decouple so that the leading-order outer nematic field is completely determined by two integrals of the incoming electric field – the intensity (conserved) and transverse momentum. The coarse-scale features of the nematic are thus demonstrated to be independent of the fine-scale details of the inner beam propagation.

Analysis of the outer problem reveals that beamline undulations are generated through initial misalignment of the incoming beam. Once off-axis, the long-range influence of the nematic boundary conditions provides an effective restoring force back towards the tube axis – which results in the undulation of the beam about the tube centerline. Analysis of the inner evolution demonstrates an extremely strong self-confinement of the beam sufficient to support the co-propagation of filamented beam structures on this finer scale.

A special waveguide case of this optical free-boundary asymptotics is presented in Section 6. However, the detailed development of the general optical free-boundary decomposition as applied to the PDE model studied here is described elsewhere [7,8].

2.3. Coupled field computations

The most important result of the optical free-boundary analysis is the identification of a critical lengthscale ($k^{-2/3}$) where the effects of self-focussing are in balance with diffraction. Roughly speaking, this is interpreted to be the transverse lengthscale associated with the beam filaments. Furthermore, in the actual experiments, which were performed prior to this analysis, the spot size of the incoming laser beam was estimated to be about 50 μm – considerably larger than the several microns to be consistent with the $k^{-2/3}$ scaling. However, despite this difference, the asymptotic theory clearly demonstrates that both the undulation and filamentation phenomena are supported within the context of the simple PDE models. The first important issue addressed by this computational study is to what extent the nematic waveguide effects, as understood within the PDE asymptotics, are robust features that persist beyond the strict assumptions of the optical free-boundary analysis.

The second issue involves the origins of the twin-filamented structure that is illustrated by Fig. 1c. Although such behavior has been computationally verified to be supported by the nonlocal paraxial evolution [8], this behavior had to be instigated through an appropriate choice of initial beam conditions. It is also possible by this nonlocal theory, that more than two filaments can be sustained. A series of computations that models the initial self-focussing of a beam entering a nematic medium seems to suggest that the creation of the twin-filamented beam structure is associated with pairs of caustics that can be created by extremely strong focussing at the first focal spot. Motivated by this hypothesis, the asymptotic construction of the special caustic waveguide in Section 6 demonstrates the coincidence that both filaments and caustics

are transverse structures at the $k^{-2/3}$ lengthscale.

3. The model equations

The computations performed here are based on a simple two-dimensional $(x\text{–}z)$ and time-independent coupled PDE model that are known, asymptotically, to support both the undulation and filamentation phenomena. Two scalar quantities, $F(x,z)$ and $\theta(x,z)$, represent the optical and nematic fields and are governed by the coupling between a parabolic wave equation and a nonlinear elliptic equation – which will be referred to as the *simple paraxial model:*

$$2ikF_z + F_{xx} + k^2\alpha \sin^2\theta\, F = 0 \tag{2}$$

$$\theta_{xx} + \theta_{zz} + |F|^2 \sin 2\theta = 0. \tag{3}$$

The x and z-coordinates identify the transverse and longitudinal directions, and the two parameters k and α denote the non-dimensionalized wavenumber and refractive anisotropy.

At the transverse boundaries $(x = \pm 1)$, Dirichlet conditions are applied to both electric and nematic fields:

$$F(x = \pm 1, z) = 0, \quad \theta(x = \pm 1, z) = 0. \tag{4}$$

The incident light field is introduced through by an initial value of $F(x, z = 0)$ for the parabolic wave evolution, the majority of the simulations use the Gaussian profile

$$F(x, z = 0) = F_0\, e^{-(16x)^2} \tag{5}$$

which models the incoming laser spot. Finally, because of the elliptic nature of the nematic PDE, boundary conditions at both longitudinal boundaries $(z = 0, L)$ are required – unless specified otherwise, these are assigned as:

$$\theta(x, z = 0) = 0, \quad \theta_z(x, z = L) = 0. \tag{6}$$

The Dirichlet condition at $(z = 0)$ simulates perpendicular anchoring of the nematic at the entry end of the capillary. The Neumann end condition at $(z = L)$ is an artificial boundary condition used to approximate a semi-infinite tube. These nematic end conditions are chosen to be in reasonable correspondence with the original experiments – a free-boundary (meniscus) at the front end of an ostensibly infinite length capillary tube.

The system (2),(3) represents a considerable simplification from any realistic model of the interaction between light and a nematic liquid crystal. But the justification for its use as a basis for investigation derives from its ancestry as an extreme form of one of the fundamental models given by the coupling of the time-harmonic vector Maxwell equation to the static Frank free-energy nematic equation [6]:

$$\nabla \times \nabla \times \boldsymbol{E} - k^2[\boldsymbol{E} + \alpha(\boldsymbol{n}\cdot\boldsymbol{E})\boldsymbol{n}] = 0 \tag{7}$$

$$\boldsymbol{n} \times [(\nabla^2\boldsymbol{n}) + (\boldsymbol{n}\cdot\boldsymbol{E}^*)\boldsymbol{E} + (\boldsymbol{n}\cdot\boldsymbol{E})\boldsymbol{E}^*] = 0. \tag{8}$$

In the above, both the electric and nematic fields are vectors and, roughly speaking, relate to the reduced model (2),(3) through the *paraxial* substitution [10]

$$\boldsymbol{E} = \begin{pmatrix} F \\ 0 \\ H \end{pmatrix} e^{ikz}, \quad \boldsymbol{n} = \begin{pmatrix} \sin\theta \\ 0 \\ \cos\theta \end{pmatrix}. \tag{9}$$

In a slowly-varying approximation based upon the large wavenumber $(k \gg 1)$ *and* small anisotropy $(\alpha \ll 1)$ the longitudinal electric field becomes negligible $(H \ll F)$ so that the electric field is characterized only by $F(x,z)$ to leading order. After the (exact) restriction to two space dimensions, the connection to the reduced scalar system (2),(3) is established for a limit of very weak nematic anisotropy $(\alpha \ll 1)$. And although in actuality, the experimental value of the anisotropy parameter was not particularly small $(\alpha \approx 0.25)$ it has been shown that more faithful asymptotic, but non-paraxial, models do not produce qualitatively different results [8,6].

The paraxial model (2),(3) contains all of the essential physics required to observe the phenomena of self-focussing, undulation and filamentation. The complex-valued paraxial equation (2) includes the effects of diffraction (F_{xx}) and nematic anisotropy $(\alpha \sin^2\theta)$ – but by its scalar nature, neglects any polarization effects. Also omitted, even within the original Maxwell equation (7), is any form of scattering

loss – which in the experiment is considered significant only over propagation distances of several millimeters (mm). The optical influence appears as the nonlinear term in the elliptic equation (3) which acts as a source of intensity-induced ($|F|^2$) nematic deformation.

The potential difficulties in computing solutions to even the simple paraxial PDE model (2),(3) can be inferred by the presence of the large wavenumber parameter k in the paraxial F-equation. The natural evolution of this PDE will tend to produce highly-oscillatory complex phase modulations in both the longitudinal and transverse directions that necessitates a very high-resolution discretization. In contrast, the nematic equation is transparent to the complex phase modulations of F and demands a less-refined resolution, but by its elliptic nature must be resolved over the full two-dimensional (x,z) domain.

4. Numerical method

The paraxial model is unusual in that it involves the mixed coupling of two classes of PDE – a parabolic wave equation for the optics and an elliptic problem for the nematic. Numerically, this requires the implementation of a mixed algorithm. In this section, we discuss the computational method used for solving the paraxial PDE (2),(3).

4.1. The functional iteration

Of the two parts of the coupled system (2),(3), it is the elliptic nature of the nematic equation which requires the majority of the computational effort. Given the nematic field $\theta(x,z)$, determining the optical field $F(x,z)$ is a direct integration of the paraxial wave evolution (2). This, in effect, allows the nematic equation (3) to be considered as a nonlinear, nonlocal elliptic problem

$$\theta_{xx} + \theta_{yy} + |F[\theta]|^2 \sin(2\theta) = 0\,, \tag{10}$$

where the optical field $F[\theta]$ can be treated as a functional of θ. The nematic field is then obtained by the natural iteration

$$\theta^{n+1}_{xx} + \theta^{n+1}_{yy} + |F[\theta^n]|^2 \sin(2\theta^n) = 0\,, \tag{11}$$

which involves the repeated solution for θ^{n+1} by Poisson inversion. The functional $F^n = F[\theta^n]$ is obtained from the paraxial equation

$$2ikF^n_z + F^n_{xx} + k^2\alpha \sin^2\theta^n F^n = 0. \tag{12}$$

This initial value problem is solved by direct integration in z for the initial condition (5). The boundary conditions (4) and (6) are also exactly applied at each stage. This functional iteration has been chosen for convenience and convergence is observed numerically. However as a referee has pointed out, more rapid convergence could have been achieved for the global iteration (11) if a Newton-type of iteration had been employed.

The Poisson inversion for θ^{n+1} from (11) involves an additional iterative procedure. The scheme used is successive over-relaxation (SOR) with Chebyshev acceleration [11]. However, rather than iterate the Poisson inversion to convergence, we find it sufficient to fix the number of SOR iterations to 100 at each step of the global iteration. Although this may be an insufficient number for good convergence at earlier stages of the global iteration, when nearer to convergence the 100 SOR iterations are more than enough for achieving adequate results. A convergence criterion for the global iteration is established in terms of the squared L^2-norm

$$E^2_\theta = \int\!\!\int |\theta^{n+1} - \theta^n|^2 \, d\xi dz < 10^{-7}\,. \tag{13}$$

Here, the variable ξ is a stretched variable introduced in the next section. Finally, extra care is required near the initial Frederiks threshold ($I \approx 1.07$) where exceptionally slow convergence rates are observed due to the proximity of the supercritical bifurcation.

4.2. The spatial discretization

Although the computing of both fields is fairly straight-forward, simultaneous resolution over the wide range of spatial scales is efficiently handled by the introduction of a non-uniform grid. It is apparent in both the experiments and our previous numerical

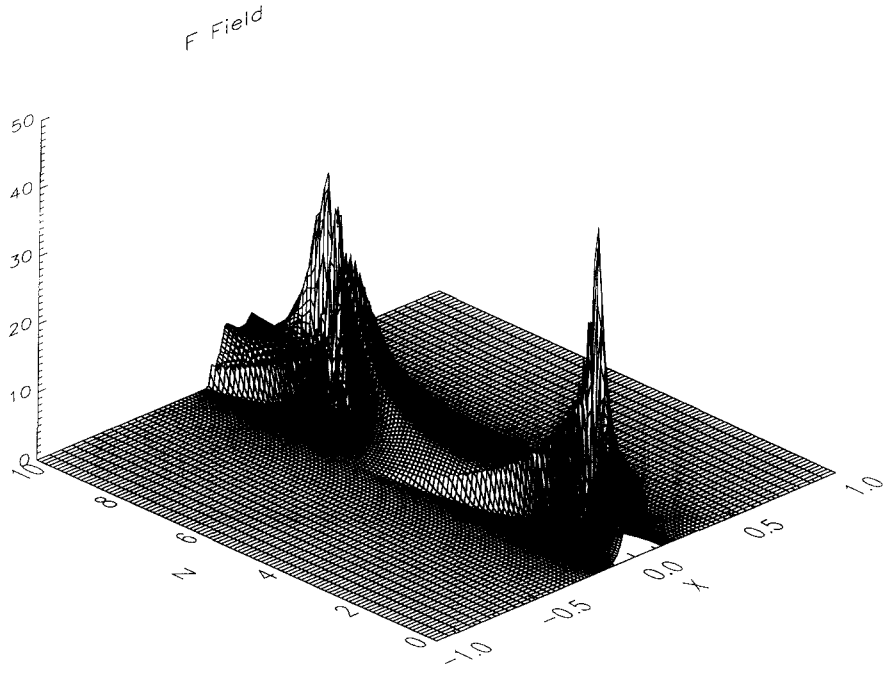

Fig. 2. Surface plot of $|F(x,z)|$ for a large intensity Gaussian (5) input beam ($F_0 = 12.0$) – the confinement of beam to the vicinity of the center axis is clearly evident.

computations [7] that the light remains confined into a beam that is typically very narrow relative to the tube width. This localization of the F-field near a central beamline motivates the use of a non-uniform grid in the transverse x-direction. For beams which propagate along the tube axis $x = 0$, the non-uniformity is implemented through a (z-independent) change of variables $x(\xi)$

$$x(\xi) = \xi[1 + q(\xi^p - 1)] , \qquad (14)$$

which for p and q constant represents a map from the interval $[-1,+1]$ onto itself. Here $0 \leq q < 1$, and $p > 1$ is an even integer. Denser grids near $x = 0$ are realized as $q \to 1$ and for larger powers p. Typical values used in the computations are $q = 0.7$ and $p = 4$. In the most extreme case, $q = 0.9$ and $p = 7$.

This change of variables with a uniform discretization in the ξ-coordinate clusters the gridpoints in the vicinity of the beamline. As a result, rewriting the paraxial model (2, 3) in terms of the new variables (ξ, z) requires only a modification of the transverse derivatives by the metric $x_\xi(\xi)$

$$2ikF_z + \frac{1}{x_\xi}\frac{\partial}{\partial\xi}\left(\frac{1}{x_\xi}F_\xi\right) + k^2\alpha(\sin\theta)^2F = 0 , \qquad (15)$$

$$\frac{1}{x_\xi}\frac{\partial}{\partial\xi}\left(\frac{1}{x_\xi}\theta_\xi\right) + \theta_{zz} + |F|^2\sin(2\theta) = 0 . \qquad (16)$$

On the line plots of Figs. 8 and 9, the non-uniform discretization of the transverse grid is indicated by marks along the top axis. Second-order finite differencing is used for the transverse ξ-derivatives, primarily on the basis of simplicity and speed considerations. The boundary conditions, as stated earlier (4)–(6), are unchanged.

The paraxial equation (15) for the field $F(\xi, z)$ is directly integrated in z by a fourth-order Runge-Kutta method, with the incoming $F(\xi, 0)$ (typically Gaussian) specified as initial data. Accordingly, the longitudinal grid size must be small enough to ensure numerical stability of the integration method, most especially at larger values of k. On the other hand, considerably less resolution is required for the elliptic θ-equation. For computational efficiency, the nematic field is solved with a moderate z-gridsize,

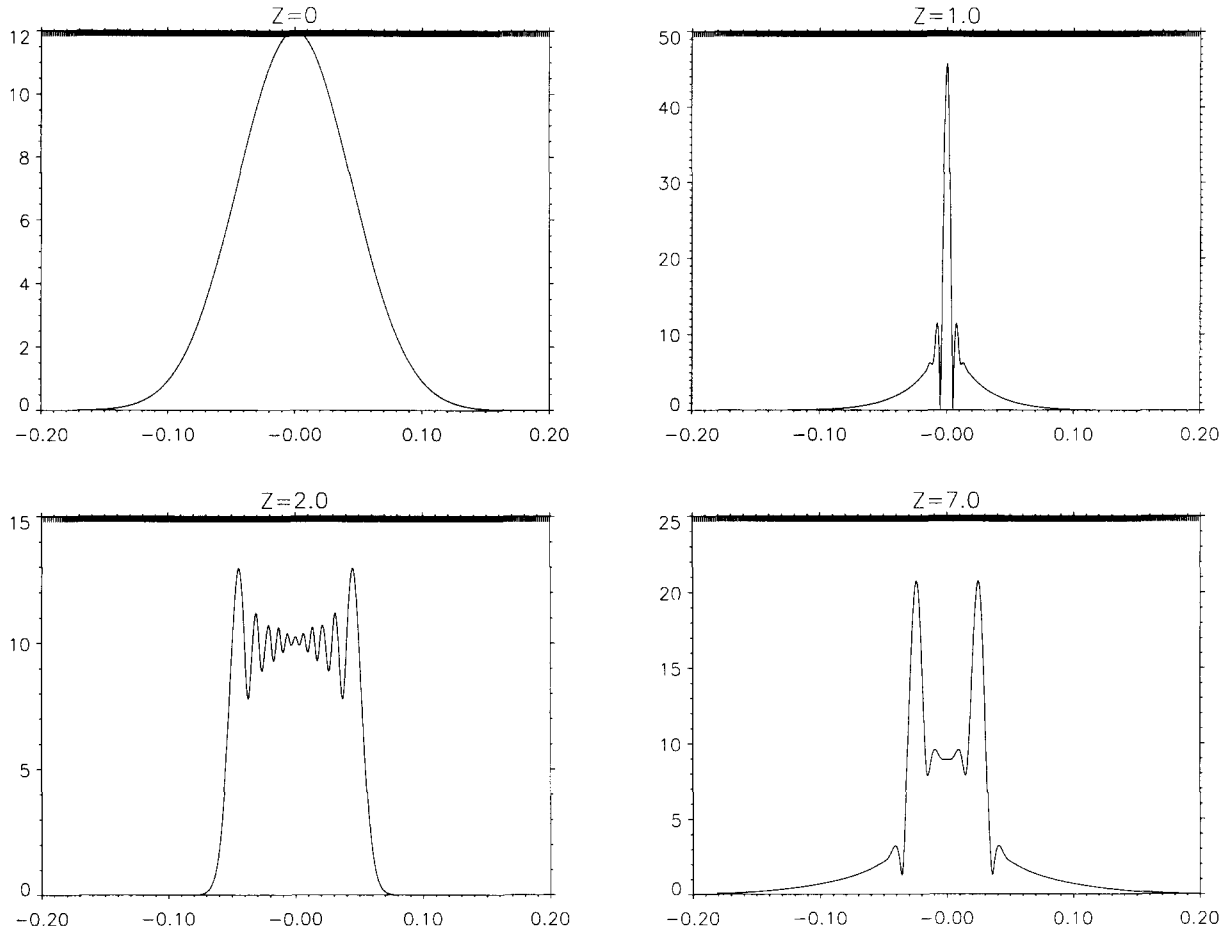

Fig. 3. Four fixed-z profiles of $|F(x)|$ for the large intensity case ($F_0 = 12.0$) – the initial Gaussian, first focal spot, and two profiles suggestive of filament/caustic-like structures.

while the optical field is evolved on a much finer sub-discretization. Values for θ at intermediate grid points are approximated from the coarser nematic grid by cubic spline interpolations. Typical runs required a factor of 60 finer discretization in z for F; at the most extreme optical intensities, factors as large as 400 were used.

Notationally we will represent the grid by $N_\xi \times N_z \times (M)$. Here N_ξ is the number of grid points in ξ, N_z the number of grid points in z for θ, and $N_z \times M$ gives the number of grid points in z for F. The longitudinal grid spacing for θ is L/N_z. And so, the factor M gives the number of additional interpolations of θ, within each such grid spacing, required for the integration of F.

4.3. Code benchmarking & verification

To illustrate the accuracy of the code, we present the results for the *most extreme* case in wavenumber ($k = 10^4$) and intensity ($F_0 = 12.0, I = 7.8$). The anisotropy is set by $\alpha = 0.1$ and the length by $L = 10$. The numerical solutions are shown as a surface plot of $|F|^2$ in Fig. 2, line plots of $|F|^2$ at four values of z in Fig. 3, and a contour plot of θ in Fig. 4c.

A simple way of reducing the computational cost is to initiate the calculation on a coarse spatial grid, then interpolate onto successively finer grids to obtain the final result. This computation is initiated on a coarse grid of size $401 \times 1001 \times (60)$. After 25 functional iterations the grid is refined to $801 \times 1001 \times (200)$. After

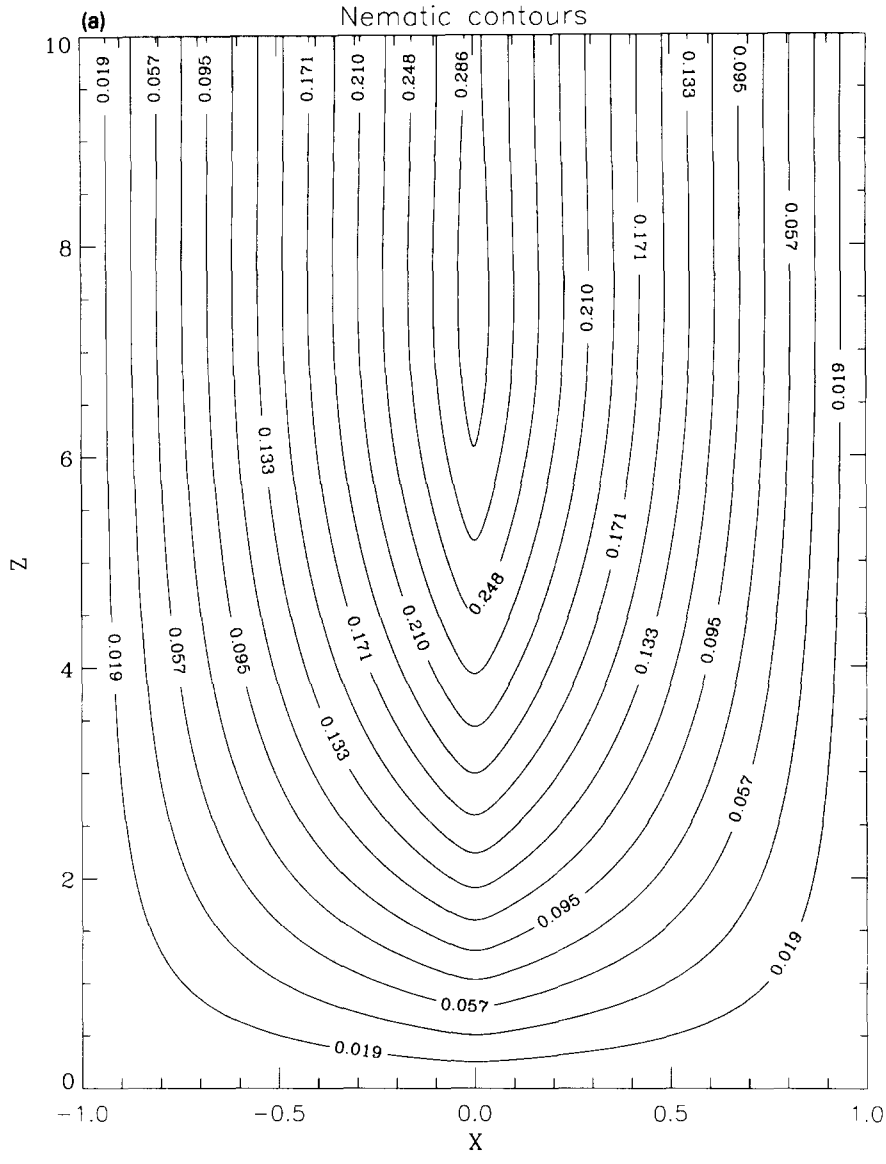

Fig. 4. Nematic contour plots of $\theta(x,z)$ for a series of input intensities (F_0 = 3.7, 7.0, 12.0). The maximum values are θ_{max} = 0.295, 1.230, 1.458.

an additional 25 functional iterations, the grid is again refined to its final resolution of $1601 \times 1001 \times (400)$. A converged solution is achieved with $E_\theta^2 = 0.9 \times 10^{-8}$. We found that a relaxation of the convergence requirement on the global iteration had very little effect on the results, suggesting that discretization error, rather than the convergence criterion, is the primary source of error.

The truncation error in the solution θ is measured in terms of both maximum and L^2-norms of the residual

$$E_{\text{res}}(\theta) = |\theta_{xx} + \theta_{zz} + |F|^2 \sin 2\theta| \,. \tag{17}$$

The maximum and L^2-norms of the residual error, E_{res}, are 5.05×10^{-3} and 4.7028×10^{-3}, respectively.

One (weak) indication of the accuracy of the z-integration of F is gotten by monitoring the conserva-

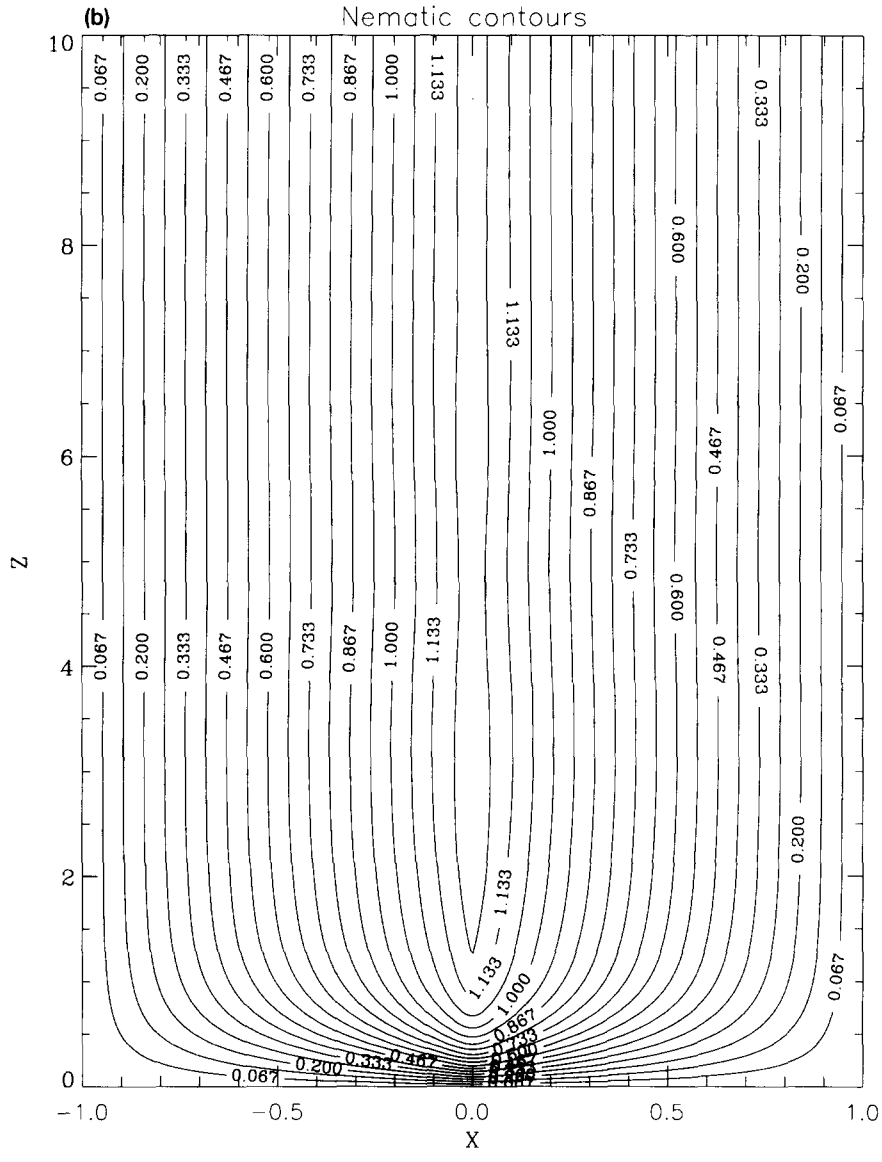

Fig. 4 — continued.

tion in z of its transverse L^2-norm, the intensity

$$I = \int_{-1}^{+1} |F(\xi, z)|^2 x_\xi \, d\xi. \tag{18}$$

For this case, we find that I is conserved to 10 digits at $z = 1$, and while the error increases monotonically as z increases, I is still conserved to over 7 digits at $z = L(= 10)$. As a more stringent test, we have used the finest mesh calculation as a base calculation from which to estimate the errors on the coarser meshes. Fig. 5 shows the relative errors of the $401 \times 1001 \times (60)$ calculation (dashed) and the $801 \times 1001 \times (200)$ calculation (solid), from the $1601 \times 1001 \times (400)$ base calculation, as a function of z. This relative error is computed as

$$E_r(z) = \frac{||F(\cdot, z) - F^*(\cdot, z)||_{L^2}}{||F^*(\cdot, z)||_{L^2}},$$

where F^* is given by the finest mesh calculation, and

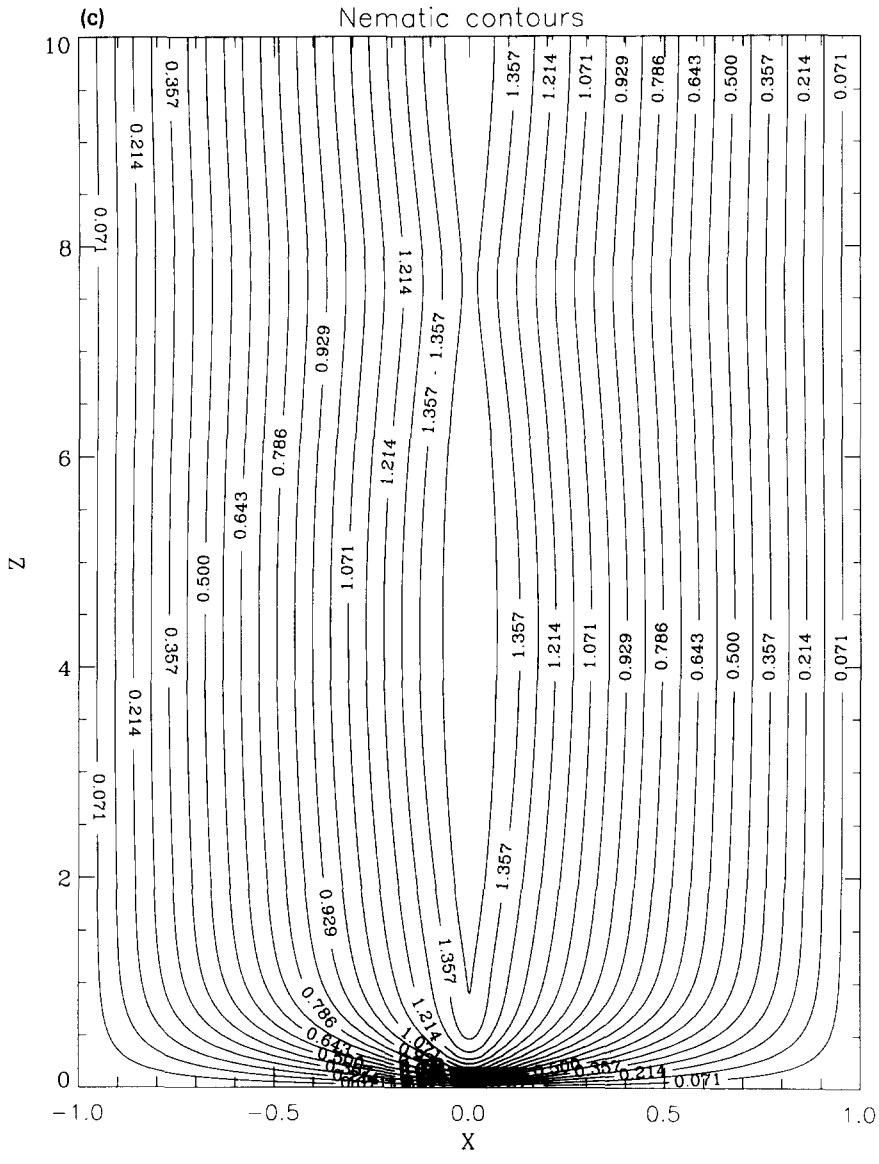

Fig. 4 — continued.

the integration is the transverse variable ξ. The functional iteration at each resolution was continued to convergence. The errors are largest at $z = L = 10$, at which there is an improvement in this L^2 error by a factor of 7 from the $401 \times 1001 \times (60)$ mesh to the $801 \times 1001 \times (200)$ mesh. This latter, intermediate mesh calculation has about 5% relative error. We emphasize that this error *does not* measure the error on the finest mesh, but does demonstrate consistency with convergence as the mesh is refined. We can very reasonably expect a yet higher accuracy on our finest mesh. And we further reiterate that this benchmarking study has been carried out for that calculation which we found the most difficult to resolve.

5. Numerical results

Three sets of numerical simulations are presented which correlate the behaviors of the paraxial

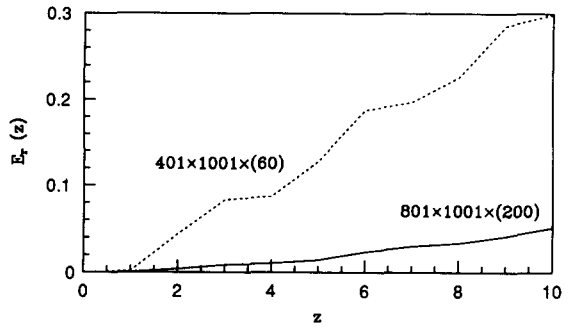

Fig. 5. The relative error E_r of the lower resolution calculations from the finest resolution calculation, for the most extreme case considered ($k = 10^4$, $F_0 = 12.0$, $I = 7.8$).

PDE model with the original experiments and free-boundary asymptotics. In the first set, the formation and behavior of focal spots is observed with increasing input beam intensity. In the second series, the development of increasingly complex structures are followed in the approach to the large wavenumber k limit. In the third set, two special solutions are reproduced. One verifies the asymptotic prediction of the nematic waveguide scale, the other demonstrates the undulation of a beam with an initial off-axis deflection.

To present the computational results, several visualization formats are used. The variations in the nematic angle $\theta(x, z)$ are shown on contour plots which correspond, in the context of this scalar Helmholtz model, to the level curves of the index of refraction. The evolution of the electric field $|F|^2$ are displayed in transverse line plots for fixed z, x–z surface plots, or in ξ–z grayscale density plots. The advantage of the grayscales are their resemblance to the actual experimental photographs – note however that they are only presented in the stretched ξ-coordinate.

5.1. *Self-focussing & filamentation*

Independent of the electric field $|F|^2$, the nematic equation (3) is always satisfied by the trivial $\theta = 0$ solution. This represents a uniform and undistorted liquid crystal state. A characteristic feature of the interaction of light with liquid crystal is a supercritical bifurcation above which a non-uniform structured state becomes energetically preferred. This symmetry-breaking is referred to as a Frederiks bifurcation [2].

The first series of computations simulates the nematic self-focussing of an incoming beam with a Gaussian profile,

$$F(x, z = 0) = F_0 \exp^{-(16x)^2} \tag{19}$$

where the beamwidth roughly corresponds to the experimental beam spot width of 50 microns. The total intensity of the beam is given by the integral

$$I = \int_{-1}^{+1} |F(x, z = 0)|^2 \, dx = \frac{F_0^2}{16}\sqrt{\frac{\pi}{2}}\,, \tag{20}$$

whose value is a constant for all values of z. The anisotropy is set to the modest value of $\alpha = 0.1$, and the wavenumber is given the relatively large value of $k = 10^4$.

Asymptotic theory for an infinitely-thin beam of finite intensity [5] predicts the critical Frederiks transition to occur at $I = 1$ ($F_0 \approx 3.6$). For these simulations, we anticipate that the transition should occur at a slightly elevated intensity due to the combined influences of the finite width of the beam and the finite longitudinal (z) nematic boundary conditions. And indeed, the computations show a transition intensity of $I \approx 1.07$ ($F_0 = 3.7$). The contour plot of the nematic distortion is shown in Fig. 4a. Just like the convex surfaces of a magnifying lens, the curved contours of the nematic angle θ result in optical focussing. The formation of a focal spot is clearly evident in the grayscale density plot of $|F|^2$ in Fig. 6a. At lower values of the field amplitude, a non-zero nematic distortion cannot be sustained and, in the absence of any index variations, the beam suffers pure diffractive broadening (not shown).

With increasing field strengths, the formation of multiple focal spots is clearly evident from the density plots as shown in Figs. 6a–c and 7a for the sequence of amplitudes $F_0 = 3.7, 3.75, 4.0$ ($I \approx 1.07, 1.10, 1.46$). Note the formation of secondary (and tertiary) focal spots that occur with the refocussing of the beam, and especially the *advance* of the focal spots towards the primary focus.

For the value of $F_0 = 7.0$ ($I \approx 3.84$), Fig. 7a shows three well-developed focal spots within the interior of

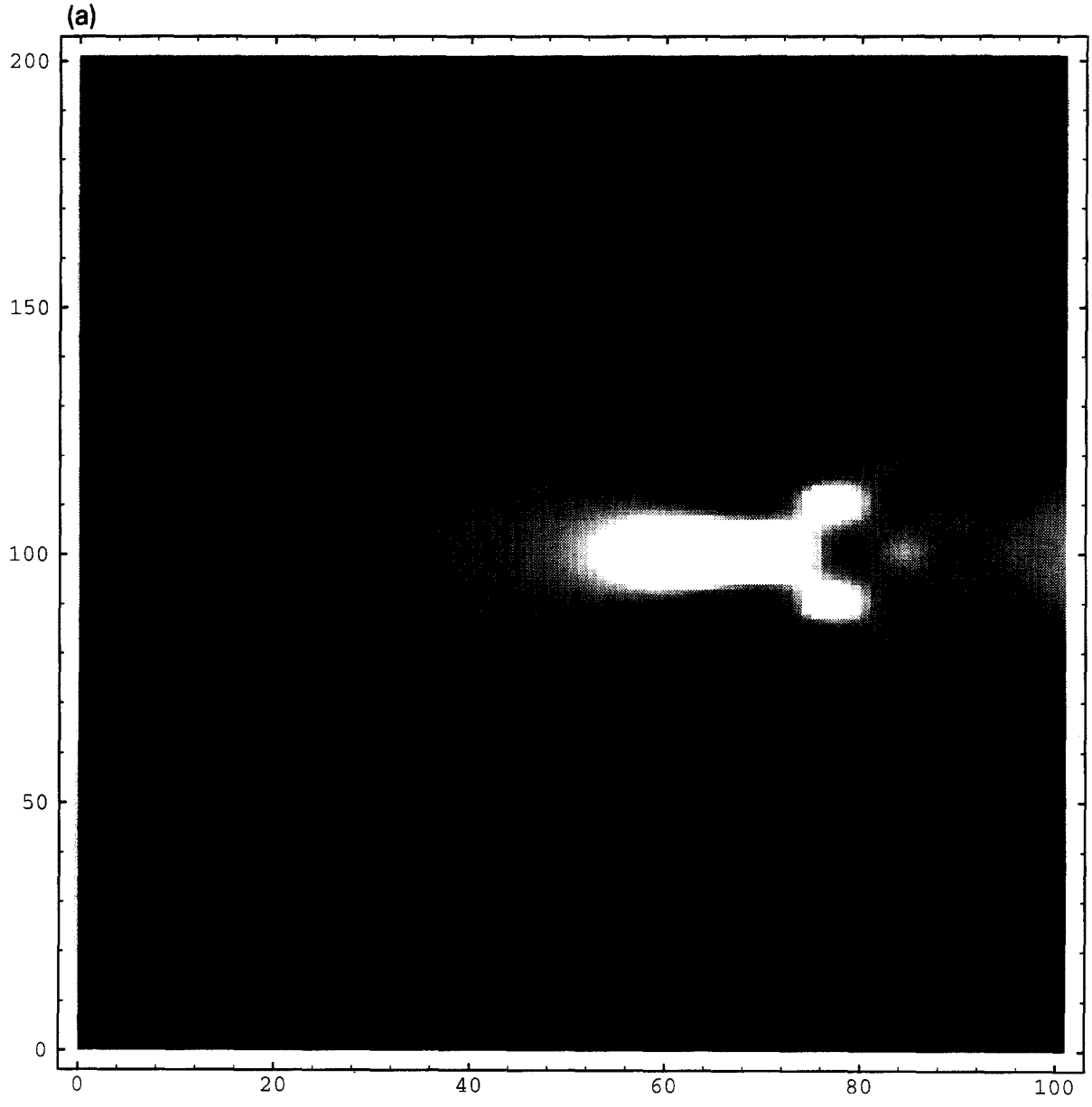

Fig. 6. Self-focussing simulations plotted as grayscale where higher intensities $|F(\xi, z)|^2$ are in white. For clarity, the axes are left in the non-uniform coordinates. As the input intensity of the initial Gaussian beam (5) is increased ($F_0 = 3.7, 3.75, 4.0$), the formation and advance of multiple focal spots is clearly seen.

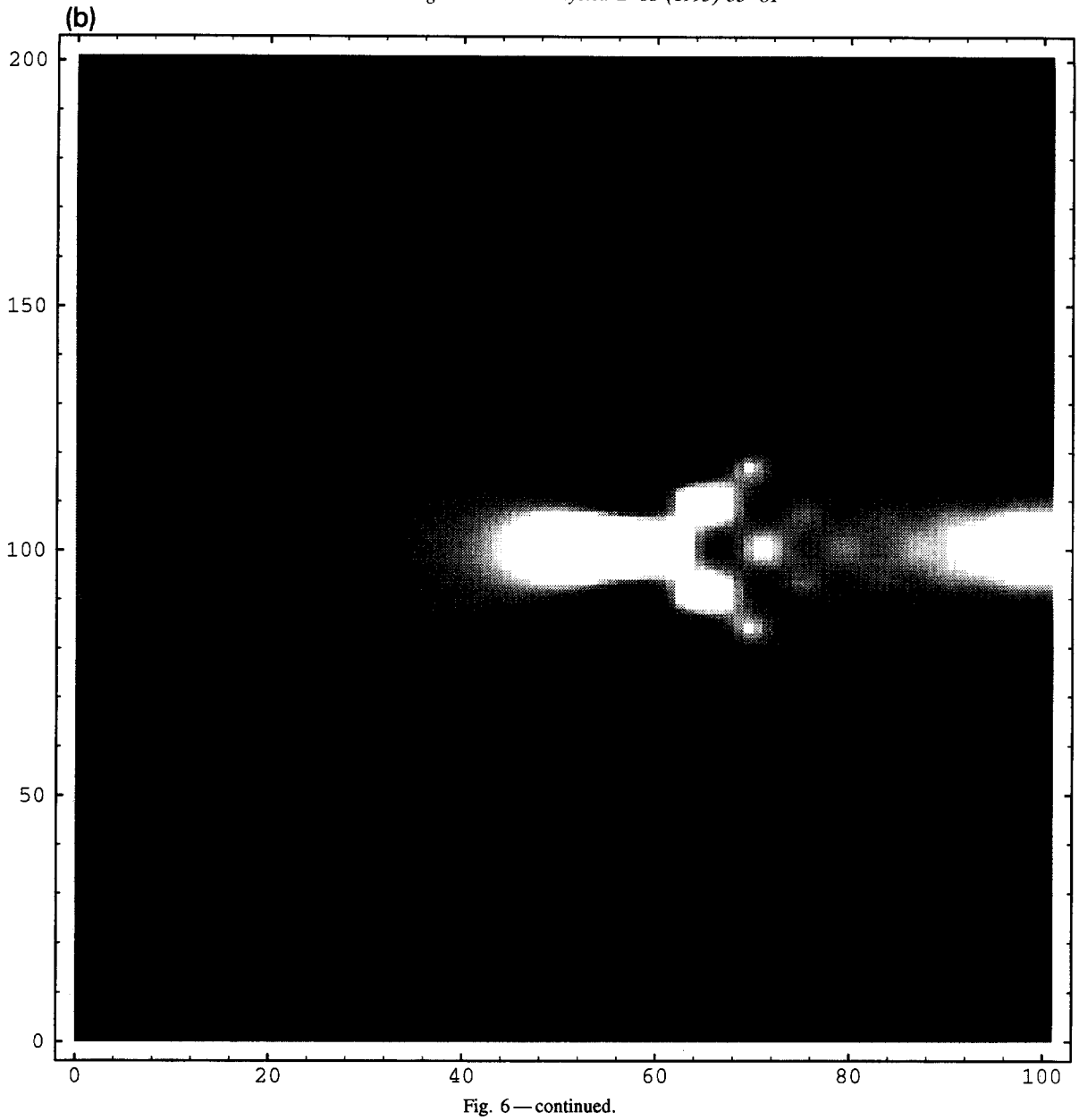

Fig. 6 — continued.

the computational domain. As the beam intensity is increased beyond this point, however, the following two crucial differences are observed: (a) the primary focal spot seems to remains at a fixed location behind the beam entry point ($z = 0$); and (b) the secondary focal spots now recede away from the primary focus. This behavior is demonstrated by the series of density plots in Figs. 7a–c which are produced for larger amplitudes $F_0 = 7.0, 9.0, 12.0$ ($I \approx 3.84, 6.34, 11.28$).

These computations suggest the following scenario as the input beam intensity is increased:

- Initially, the amount of nematic distortion increases as does the focussing – this results in the forward advance of all focal spots.
- Eventually the refractive effects of $\sin^2\theta$ saturate and the advance of the primary focal spot becomes limited by the creation of the front-edge nematic boundary layer apparent in Figs. 4b,c.

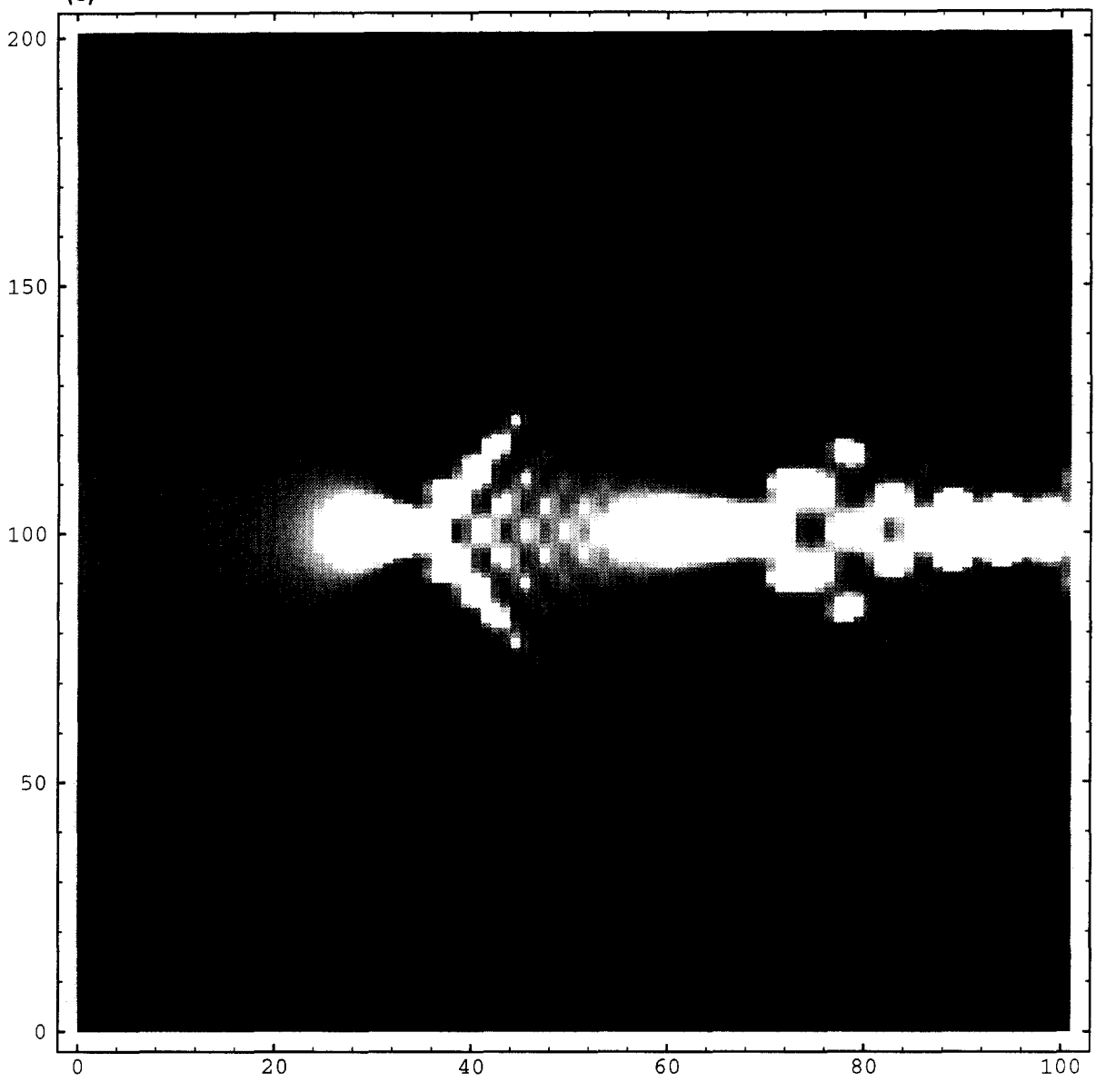

Fig. 6 — continued.

- Beyond this point, the increased focussing serves only to generate strong caustics exiting the primary focus – their resemblance to filaments is suggested by comparing Fig. 1c with Fig. 7b,c.
- The extreme transverse divergence of these caustics after the primary focus requires longer propagation distances between subsequent refocussings and results in the recession of the secondary foci.

It is also noteworthy that, like the experimental filaments, the numerical appearance of these caustics only occur for intensities well beyond the initial Frederiks threshold. Furthermore, the experiments also report that the characteristic length between successive focal spots exhibited the same advance-to-recession transition when filament crossings are interpreted as refocussings [4].

This correlation between the computations and the experiments provides the most compelling, albeit

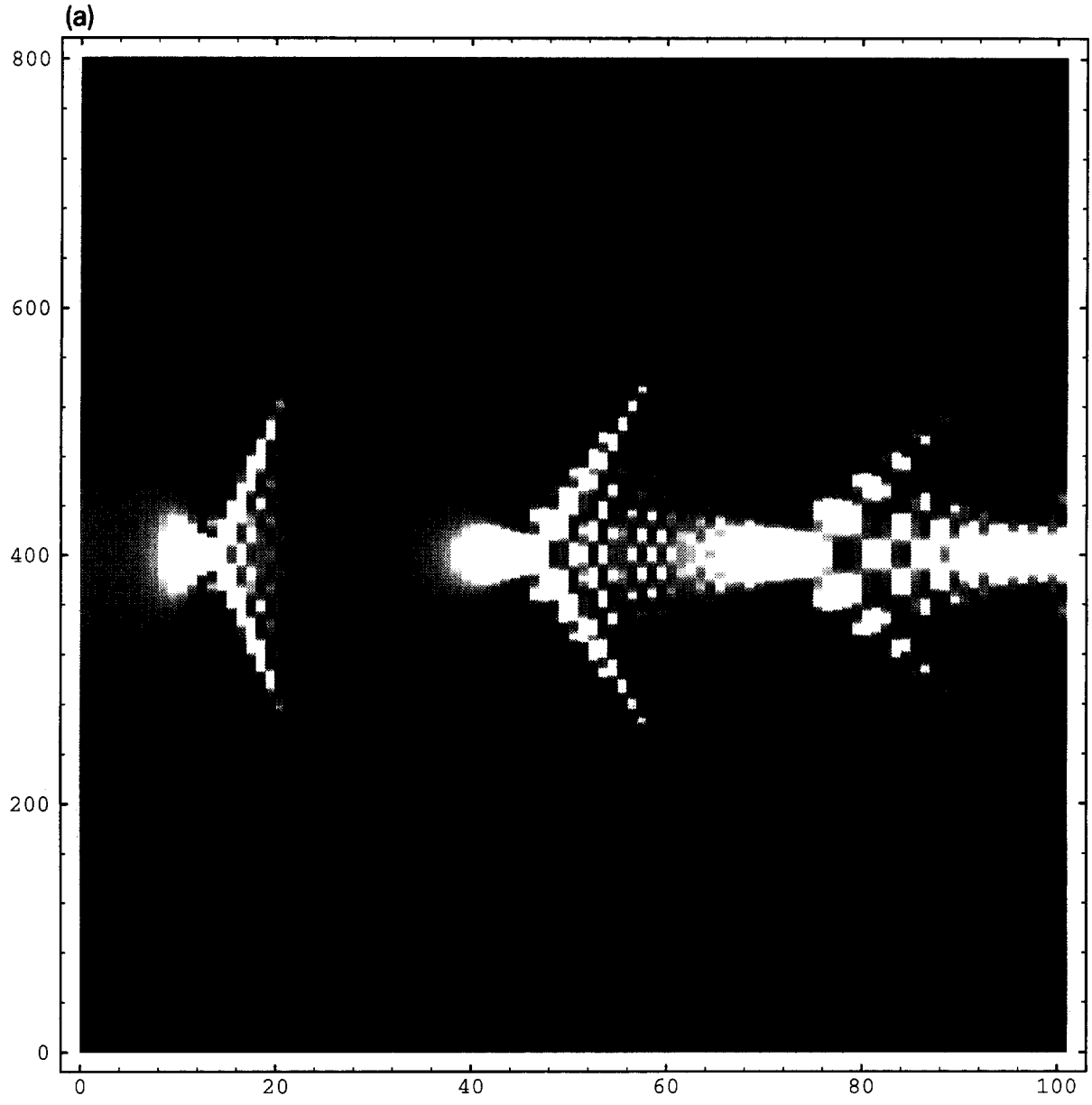

Fig. 7. Grayscale plots of $|F(\xi, z)|^2$ like those of Fig. 6, but for higher intensities ($F_0 = 7.0, 9.0, 12.0$). The formation of strong caustics is clearly demonstrated as well as the recession of secondary focal spots.

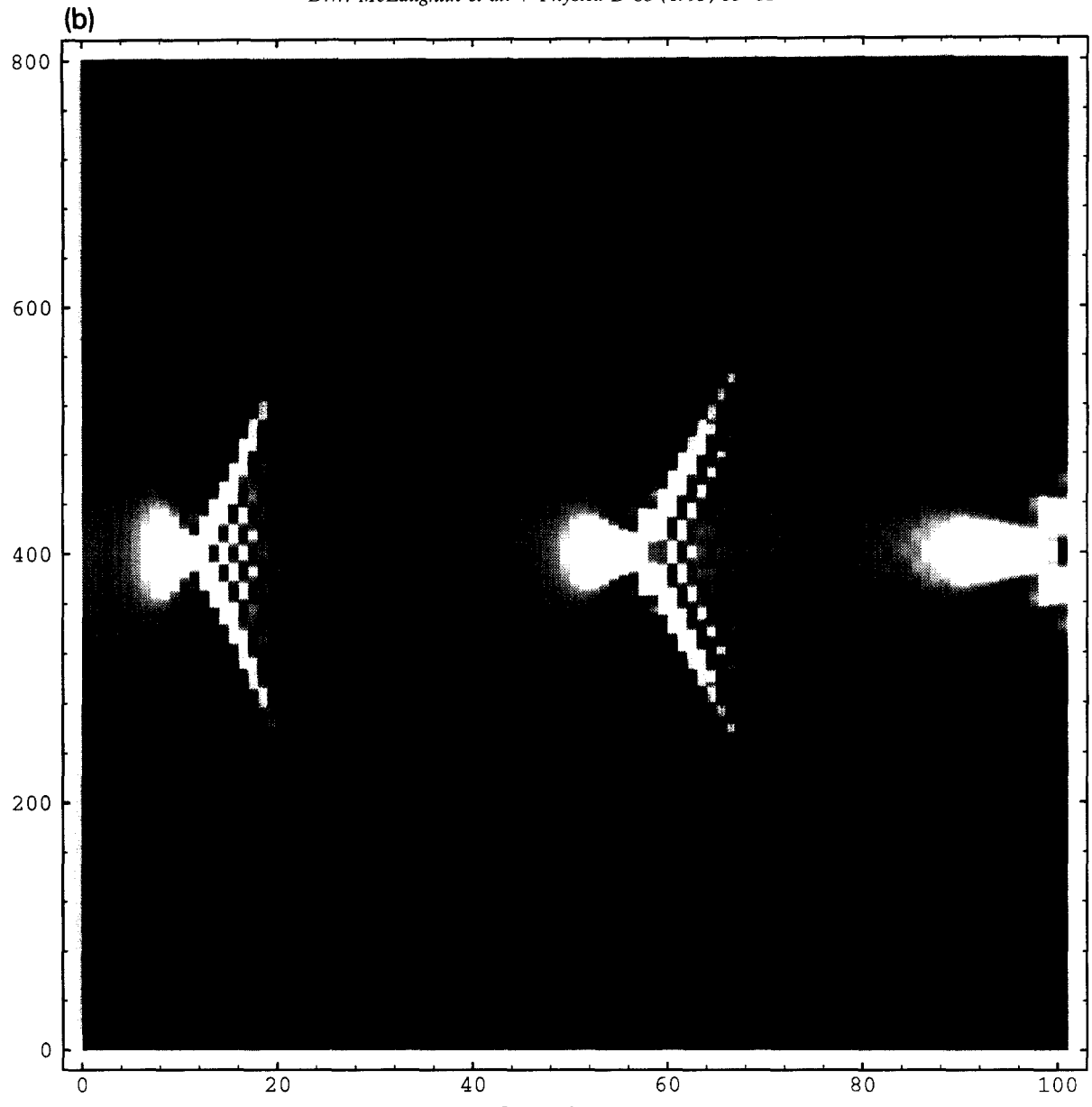

Fig. 7 — continued.

somewhat circumstantial, evidence that the mechanism by which beam filaments form is intimately linked to the creation of a caustic pair under the extreme self-focussing of the beam.

This suggested connection of filaments with caustics in the PDE system (2),(3) is further supported by an asymptotic discussion of two special waveguide solutions. These solutions – one which is filament-like, the other caustic-like – are shown in Section 6 to be both characterized by the $k^{-2/3}$ lengthscale.

5.2. *Fine-scale structure*

A key result of the optical free-boundary asymptotics is the identification, through significant balance arguments, of a critical transverse length that scales on $k^{-2/3}$. A sequence of four focussing simulations were performed for wavenumbers spanning $k = 4000$–

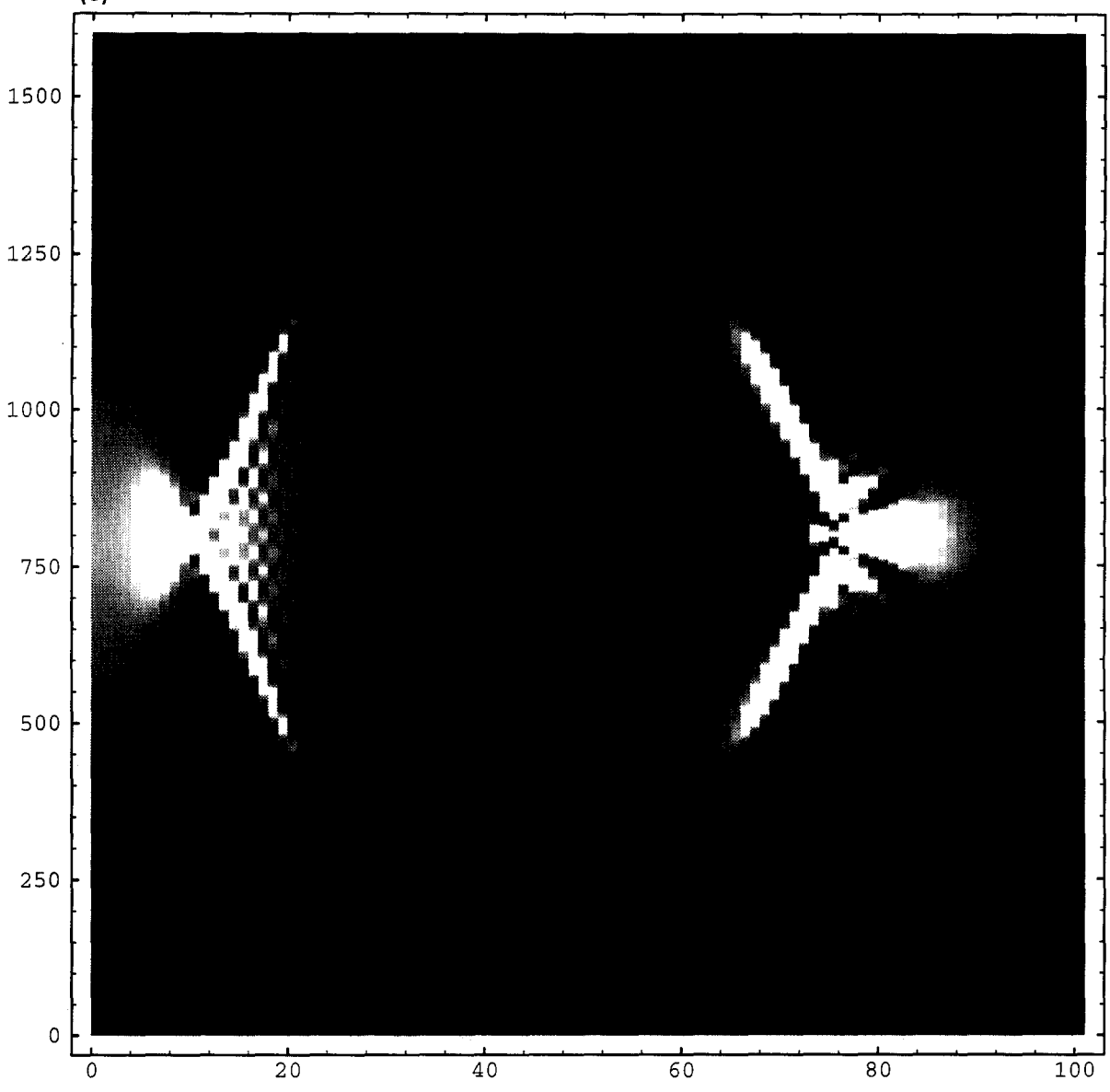

Fig. 7 — continued.

10000. Although the range of wavenumbers available to our computational resources was insufficient to positively detect a $k^{-2/3}$ dependence, Figs. 8 and 9 clearly indicate an increase in the fine-scale structure with wavenumber at two fixed longitudinal positions. On more careful inspection, the nematic profiles for all four runs are virtually identical (over all values of z, not just those shown), and the same might be said in the gross features of the $|F|^2$ envelope profiles.

5.3. Beam undulation

Fig. 10a illustrates the propagation (in z) of a simple waveguide eigenmode. The asymptotic calculation of this solution to the paraxial PDE model is sketched in Section 6. The unchanging nature of this self-trapped beam is due to the exact balance between diffraction and the nonlinear focussing.

When the $x \to -x$ symmetry of this initial condi-

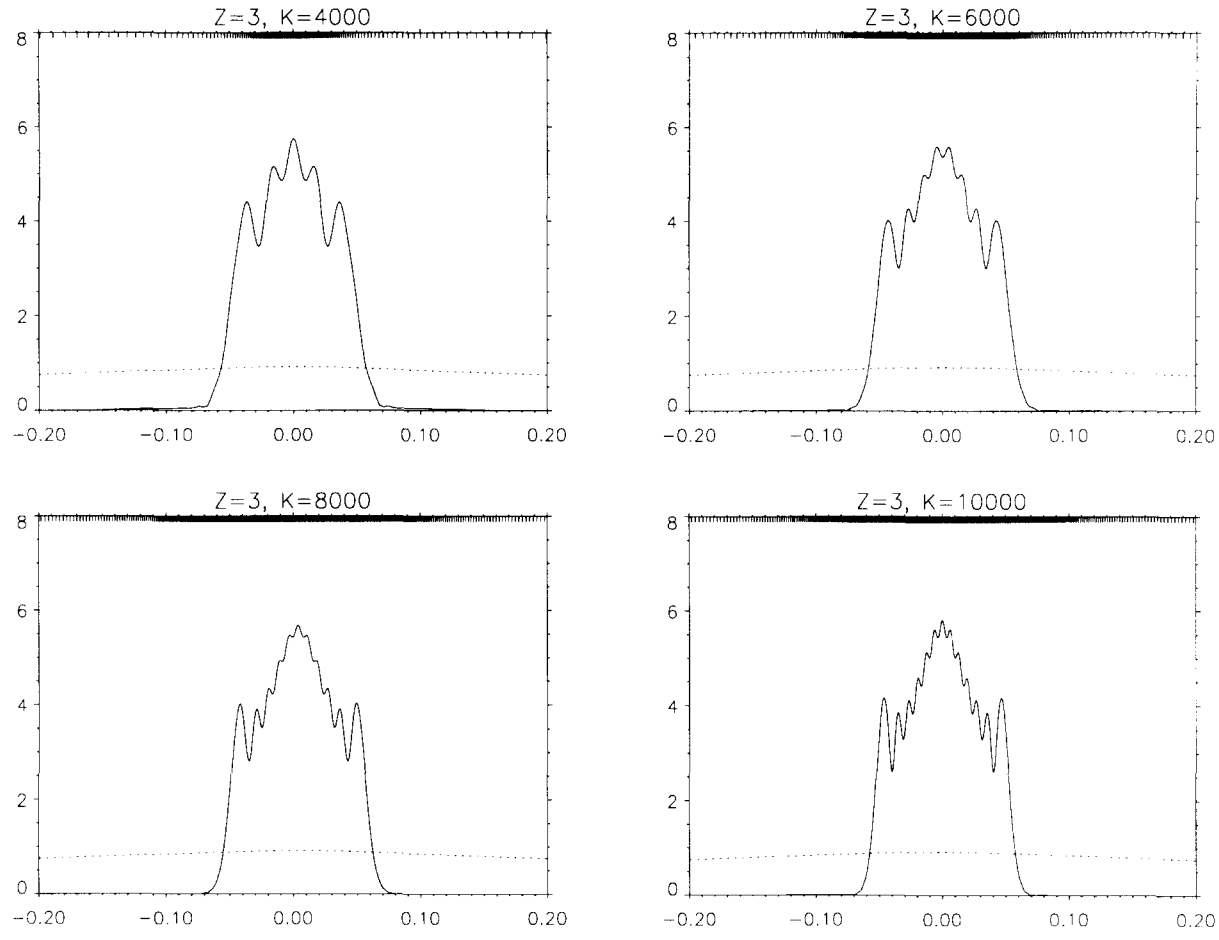

Fig. 8. Transverse line plots of $|F(x)|$ for an initial Gaussian beam (5) at fixed input intensity and longitudinal position ($F_0 = 5.0, z = 3.0$). These plots suggest a similarity of the envelopes over the four values of wavenumber ($k = 4, 6, 8, 10 \times 10^3$) shown.

tion is broken by a multiplicative factor of e^{icx}, where $c \neq 0$ imparts an initial transverse momentum, the resulting evolution is the off-axis undulation shown in Fig. 10b ($c = 50$). In the experiments, non-zero transverse beam momentum is naturally introduced when the optical polarization vector interacts with the broken $\theta \rightarrow -\theta$ symmetry of the nematic that occurs at the Frederiks transition.

This computation provides a numerical confirmation of the primary result of the free-boundary asymptotic analysis. These asymptotics construct a self-confined paraxial beam that follows an undulating ray path through the nematic medium – this is precisely the situation that is demonstrated by Fig. 10b. Furthermore, although the domain length ($L = 20$) is insufficient to capture a full period of the undulation, it appears that its wavelength is on the order of 15–20. This value is consistent with the asymptotic free-boundary predictions [5].

6. Nonlinear eigenmodes

The computations suggest that filaments may be naturally created by focussing caustics. One characteristic feature of a filament is that its transverse width scales on $k^{-2/3}$ and is determined by a critical balance between diffraction and nonlinear self-focussing. Although a general caustic analysis for the paraxial model seems unlikely, a special caustic solution can

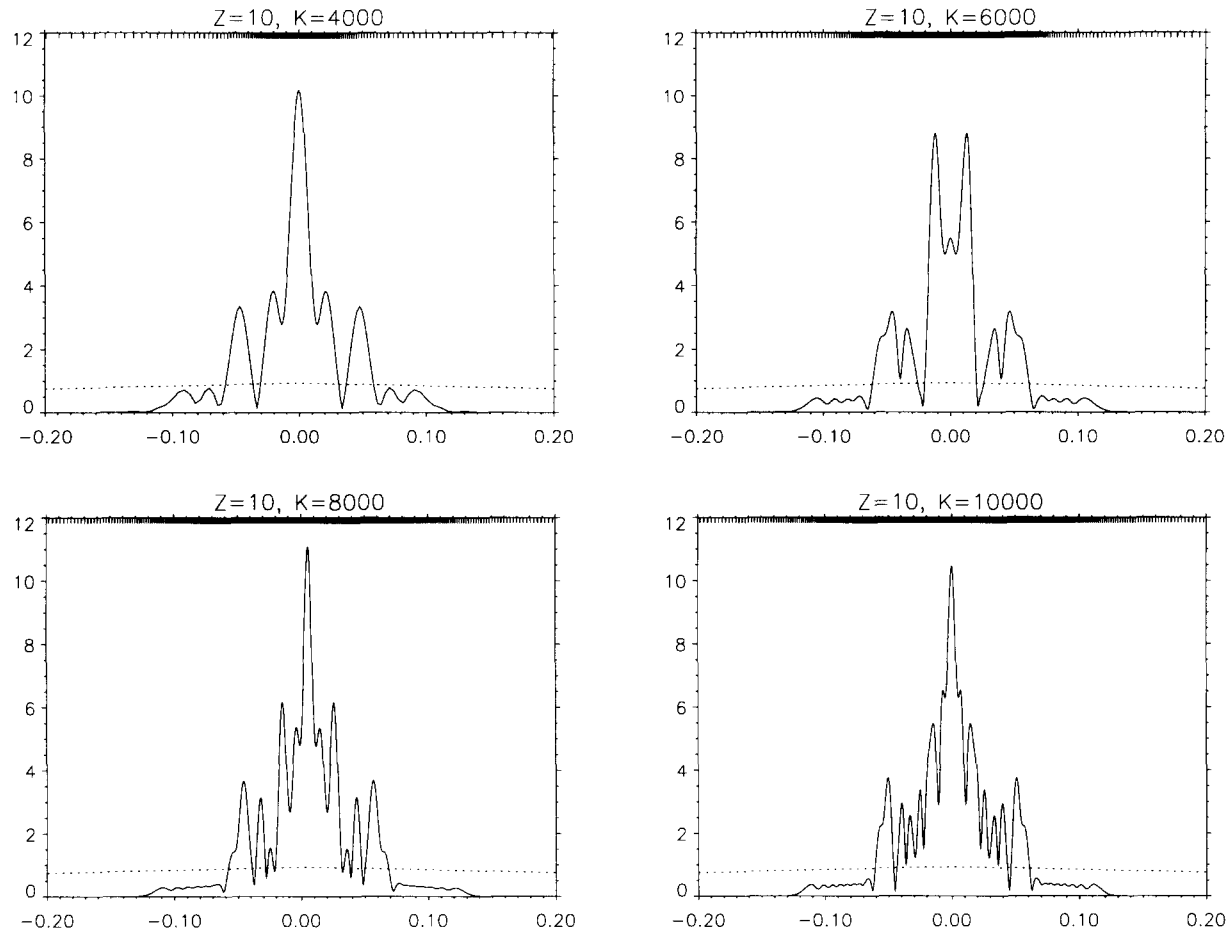

Fig. 9. Line plots of $|F(x)|$ like those of Fig. 8 but for $z = 10$. This similarity of envelopes over varying k is apparent for any fixed longitudinal position z.

be constructed asymptotically and also occurs at the same $k^{-2/3}$ scale. The two analyses that follow essentially construct two extremes of waveguide modes: the first is narrow and resembles a single filament, the second is broad and possesses caustic fringes.

Consider solutions of the paraxial PDE model where both the optical intensity $|F|^2$ and the nematic angle θ are independent of z

$$F(x,z) = f(x)\, e^{ik\mu z}, \quad \theta(x,z) = r(x), \tag{21}$$

where the constant μ plays a rôle as a nonlinear eigenvalue. The transverse profiles $f(x)$ and $r(x)$ satisfy the *real* ODE boundary-value problem

$$f'' + k^2\,(\alpha \sin^2 r - 2\mu)\, f = 0,$$
$$r'' + f^2 \sin 2r = 0,$$
$$\text{with } f(x = \pm 1) = r(x = \pm 1) = 0 \tag{22}$$

as obtained from direct substitution of (21) into the paraxial model (2),(3). The basic character of this ODE eigenvalue problem is that of a Schrödinger equation for f whose potential r is itself determined by a nonlinear coupling to f^2. In the limit of large wavenumber k, two types of solutions are constructed – one resembling a single filament, and the other a broad eigenmode delineated by two turning points (caustics). The key result is that the $k^{-2/3}$ spatial scale of the single filament exactly matches the scaling found locally at the caustic turning points – asymptotic evidence that supports the evolution of

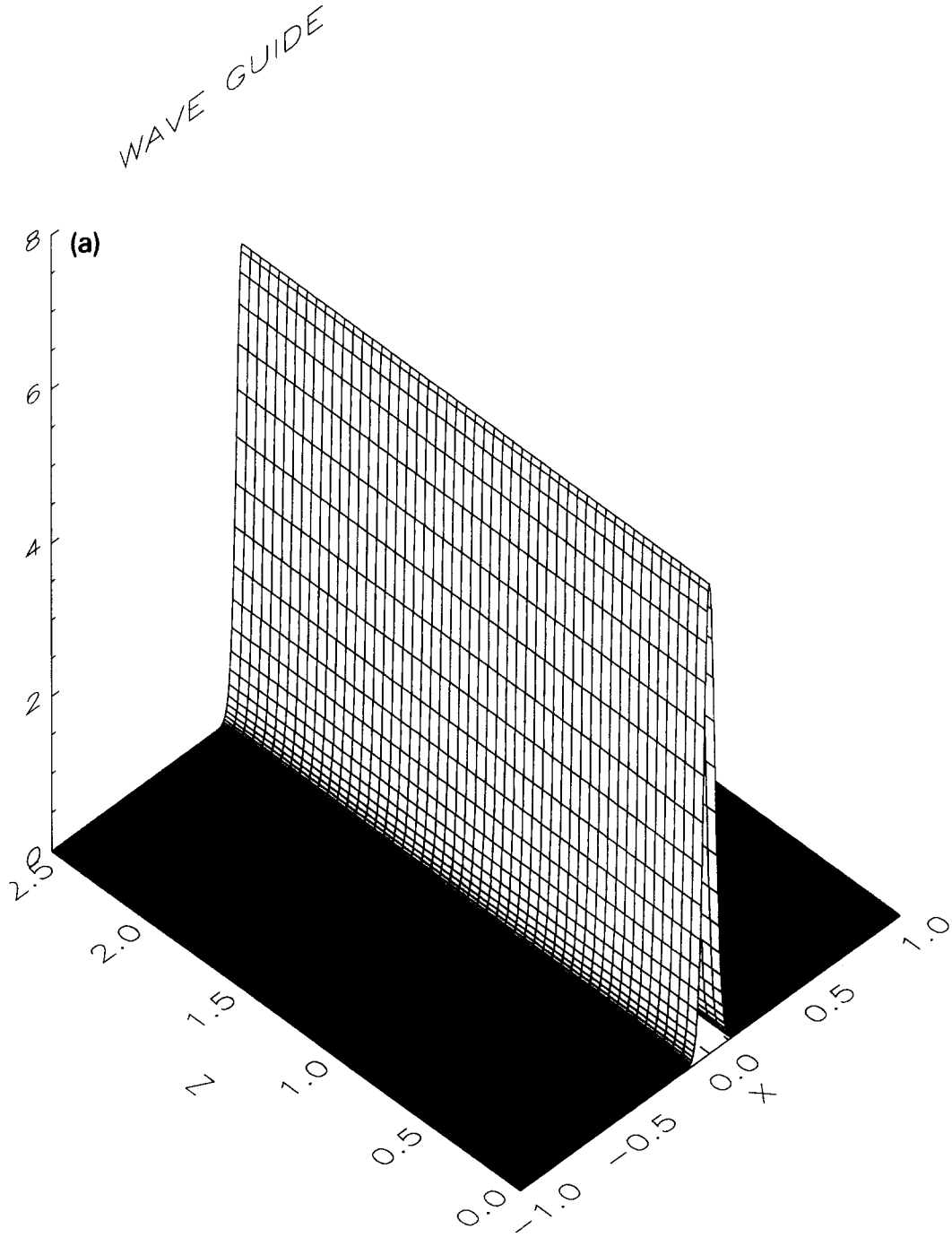

Fig. 10. (a) PDE simulation initialized to the filament solution of the ODEs (22) with $I \approx 1.96$. Note that the nematic boundary at $z = 0$ is set to the ODE solution and not to $\theta = 0$. (b) PDE simulation of an undulating beam. The initial condition is the filament of (a) with some transverse momentum introduced through an additional factor of e^{icx} in the F-field.

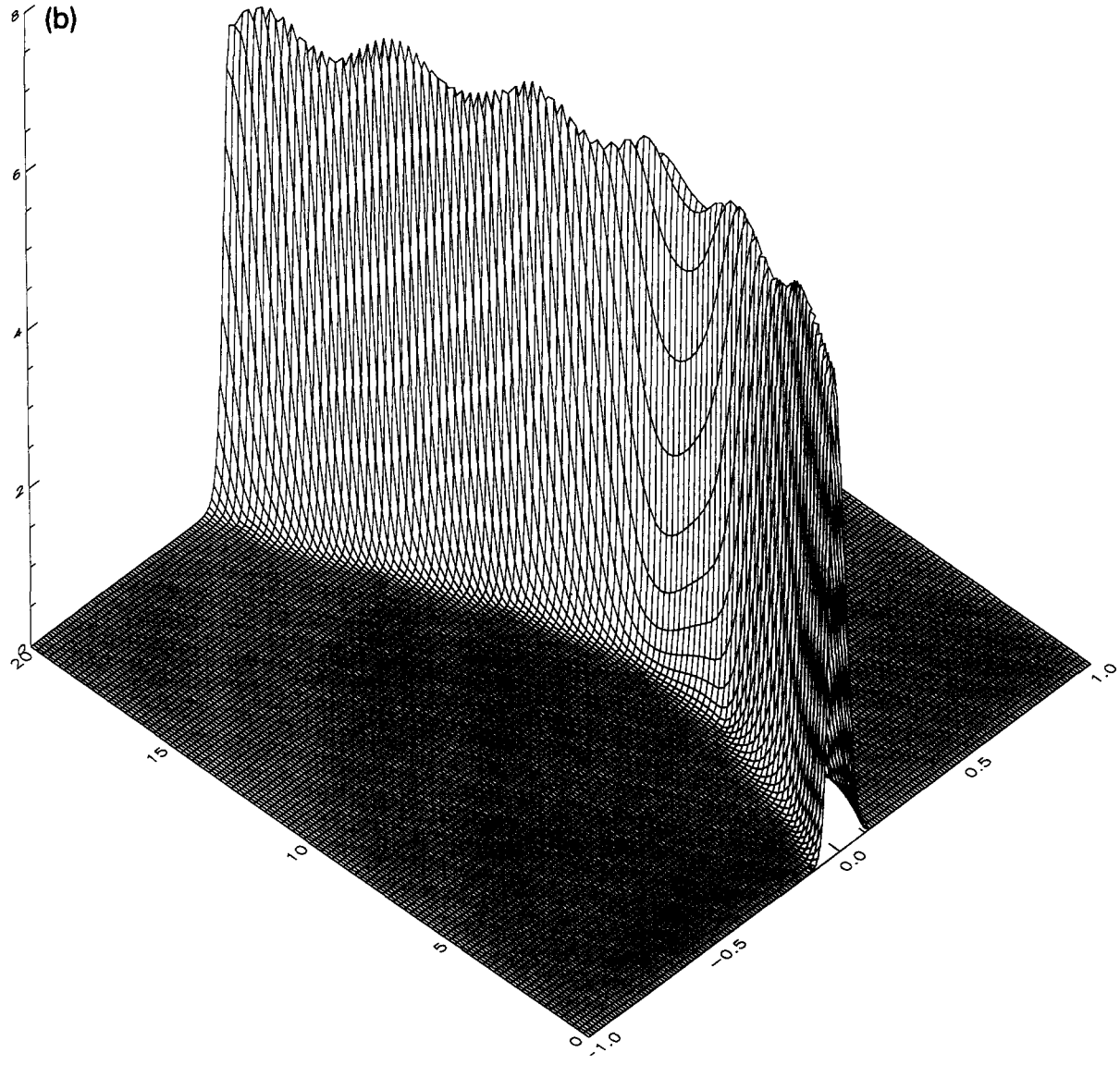

Fig. 10 — continued.

filaments from focussing caustics.

6.1. Simple filament scaling

The following asymptotic construction for this simple eigenmode is a special case of the optical free-boundary method. A numerically obtained solution is shown in Fig. 11 for the value of $k \approx 1000$. For large k the optical energy is assumed to be strongly confined near $x = 0$ so that away from the origin f is exponentially small. Since f is ostensibly zero, the nematic r has the piecewise linear *outer representation* for $x \neq 0$:

$$\begin{aligned} &f \sim \text{exponentially small}, \\ &r \sim R_0 (1 - |x|), \end{aligned} \tag{23}$$

which satisfies the homogeneous Dirichlet boundary conditions and continuity, but at $x = 0$ has derivative jump. This discontinuity can be interpreted as the optical beam f having a delta-function transverse profile in the $k \to \infty$ limit. The derivative jump is smoothed

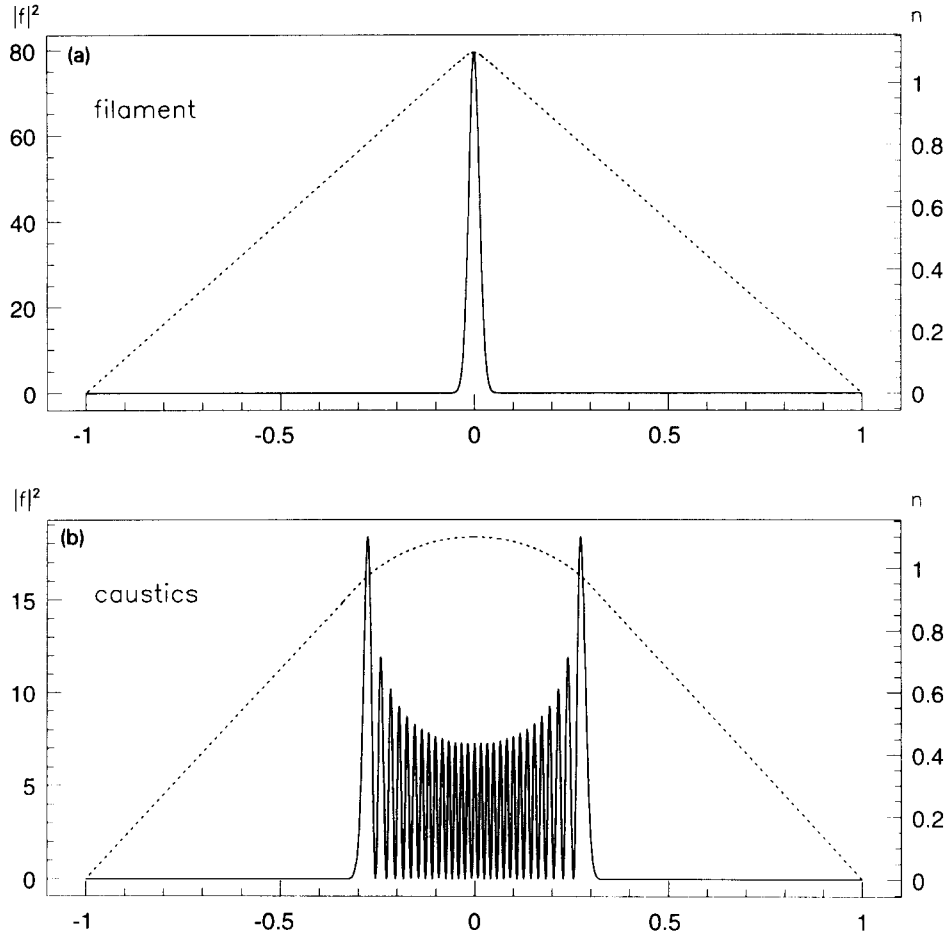

Fig. 11. Two special waveguide solutions of the paraxial PDE model that are obtained by solving the nonlinear eigenvalue problem (22). Note the similarity between the (a) filament and the largest peak of the (b) caustic.

by introducing a fine lengthscale

$$\bar{x} = \gamma\, x \tag{24}$$

that resolves the optical-layer solution in the vicinity of the origin. The parameter γ is a large scaling parameter whose dependence on k is determined by asymptotic matching.

Within the narrow optical-layer, the following perturbation expansions are used:

$$\begin{aligned} f &\sim \sqrt{\gamma}\, \bar{f}(\bar{x}), \\ r &\sim R_0 + \frac{1}{\gamma}\, \bar{r}(\bar{x}), \\ \mu &\sim \frac{\alpha}{2}\left(\sin^2 R_0 + \frac{1}{\gamma}\, \sin 2R_0\, \bar{\mu}\right), \end{aligned} \tag{25}$$

where it is essential that the amplitude of $\bar{f}$ be rescaled in a manner that preserves the $O(1)$ integrated intensity. The nematic correction term $(\bar{r})$ effects a smooth connection between the outer linear asymptotes (23). Direct substitution into the ODEs (22) gives to leading-order, a modified nonlinear eigenvalue problem

$$\begin{aligned} &\bar{f}'' + \frac{k^2}{\gamma^3}\, \alpha\, (\sin 2R_0)\, (\bar{r} - \bar{\mu})\, \bar{f} = 0, \\ &\bar{r}'' + (\sin 2R_0)\, \bar{f}^{\,2} = 0, \end{aligned}$$

$$\text{with} \quad \begin{aligned} \bar{f}(\bar{x} = \pm\infty) &= 0, \\ \bar{r}(\bar{x} \to \pm\infty) &\sim \mp R_0\, \bar{x} \end{aligned} \tag{26}$$

which balances all of the *inner corrections* $\bar{f}$, $\bar{r}$ and $\bar{\mu}$ provided the parameter γ is chosen to be

$$\gamma \sim (k^2\alpha \sin 2R_0)^{1/3}. \tag{27}$$

Devoid of the large k parameter, numerical eigensolutions for (26) are readily obtained – Fig. 11 ($k \approx 10^3$) and the initial conditions for the PDE computation of Fig. 10a ($k = 10^4$) were generated in this manner.

Note that the inhomogeneous nematic condition at infinity guarantees a consistent asymptotic match to the outer solution (23). Moreover, a necessary condition on the eigensolutions is obtained by direct integration of the $\bar{r}$-equation (26)

$$I \equiv \int_{-\infty}^{+\infty} \bar{f}^2(\bar{x})\, d\bar{x} = \frac{2R_0}{\sin 2R_0} \geq 1 \tag{28}$$

which reproduces the unity Frederiks threshold for this special class of solution.

But of most importance is the conclusion that simple filament structures are created by the balance between diffraction and nonlinear self-focussing which occurs at the $k^{-2/3}$ spatial scale.

6.2. Special caustic scaling

This asymptotic construction of an extended eigenmode is a nonlinear adaptation of the WKBJ expression of an eigenfunction with two turning points. A numerically-generated solution of (22) for $k \approx 1000$ in Fig. 11 clearly illustrates an interior oscillatory regime terminated by a pair of turning points, or caustics. In comparison to linear Schrödinger WKBJ, the analysis here requires modification for both the nonlinearity and the separation of scales between the f and r components.

For large wavenumber k, the solutions in the oscillatory region are characterized by two scales

$$x \quad \text{and} \quad \Psi \sim k\psi(x) \tag{29}$$

where Ψ constitutes the scale of the rapid oscillations which also has a weak variation in x. The nonlinear geometrical optics begins from asymptotic expressions for the f and r components

$$f \sim A(x)\, \mathcal{S}(\Psi(x)),$$
$$r \sim R(x) + \frac{1}{k^2}\mathcal{R}(\Psi(x), R(x), A(x), \psi'(x), \ldots) \tag{30}$$

and results in slow-scale averaged equations for the envelope A and mean R. The f-field is an amplitude/phase representation where $\mathcal{S}$ is a 2π-periodic sinusoid in the unscaled phase $\Psi = O(k)$. The r-field is a near-identity decomposition where $\mathcal{R}$ contains 2π-periodic and *zero-mean* fluctuations on the scale of the rapid phase. These fluctuations are not visible in Fig. 11, but are clearly discerned for smaller values of k. In addition, we restrict this construction to solutions for which the mean R has even symmetry about the origin.

The key to the above representations is that the x-dependence is now completely imbedded into the three quantities $A(x)$, $R(x)$ and $\psi(x)$. Direct substitution of the expressions (30) into the ODEs (22) results in the two perturbation series

$$\begin{aligned}[\psi'^2 A]\{\mathcal{S}_{\Psi\Psi} + \mathcal{S}\} &\sim [(\psi'^2 - \alpha\sin^2 R + 2\mu)\, A]\, \mathcal{S} \\ &\quad - \frac{1}{k}[2\sqrt{\psi'}(\sqrt{\psi'}A)']\, \mathcal{S}_\Psi + O\left(\frac{1}{k^2}\right)\end{aligned} \tag{31}$$

$$\begin{aligned}[\psi'^2]\{\mathcal{R}_{\Psi\Psi}\} + [A^2(\mathcal{S}^2 - \tfrac{1}{2})\sin 2R] \\ \sim -[R'' + \tfrac{1}{2}A^2 \sin 2R] + O\left(\frac{1}{k}\right)\end{aligned} \tag{32}$$

where the left-hand sides constitute ODEs in Ψ for the rapidly fluctuating $\mathcal{S}$ and $\mathcal{R}$. Note that the square-bracketed factors are all independent of the rapid variable Ψ.

Periodic solutions for $\mathcal{S}$ and $\mathcal{R}$ which satisfy the left-hand sides of (31) and (32) are given by

$$\mathcal{S} \sim \begin{cases} \cos\Psi & \text{(even symmetry)} \\ \sin\Psi & \text{(odd symmetry)} \end{cases}$$

$$\mathcal{R} \sim \frac{A^2 \sin 2R}{4\psi'^2}\{\tfrac{1}{2} - \mathcal{S}^2\} \tag{33}$$

where $\mathcal{R}$ has zero-mean by virtue of $\mathcal{S}$ having a mean-square of $1/2$.

By the sinusoidal nature of $\mathcal{S}$, both $\mathcal{S}$ and $\mathcal{S}_\Psi$ perturbations on the right-hand side of (31) will result

in secular-in-Ψ growth unless both terms are zero to (at least) $O(1/k^2)$. These solvability conditions essentially yield the eikonal and transport relations of linear WKBJ theory, but as a manifestation of the nonlinearity, are not decoupled. Finally, the constant-in-Ψ perturbation on the right-hand side of (32) will not preserve the zero-mean property of $\mathcal{R}$ unless this term also vanishes. This establishes a condition for the nematic average $R(x)$.

These solvability conditions – eikonal, transport and nematic average – yield three relations that determine the slowly-varying quantities $\psi'(x)$, $A(x)$ and $R(x)$

$$\psi' \sim \sqrt{\alpha \sin^2 R - 2\mu} > 0 \tag{34}$$

$$A^2 \sim \frac{\psi_0'}{\psi'} A_0^2 \tag{35}$$

$$R'' \sim -\frac{A^2}{2} \sin 2R \tag{36}$$

which can be shown to be nominally correct to $O(1/k^2)$. The subscript 0 denotes initial values at $x = 0$. The above ODE system (although it may be argued that only the final equation truly constitutes a differential relation) possesses the first integral

$$\alpha (R')^2 - 2A_0^2 (\psi_0' - \psi') \psi_0' = 0 , \tag{37}$$

where this expression assumes the even symmetry of R by taking $R_0' = 0$. By (34), the vanishing of ψ' defines the conditions for a turning point at $x = \pm x_T$ with the associated values

$$R_T = \sin^{-1} \sqrt{\frac{2\mu}{\alpha}}, \quad R_T' = \mp \sqrt{\frac{2}{\alpha}} \psi_0' A_0 \tag{38}$$

that are obtained from (34) and the first integral (37). The vanishing of ψ' in the transport equation (35) also requires that the amplitude A^2 diverge to infinity at the turning point. This signature behavior of a caustic is resolved by a rescaling local to the turning points.

As in the previous filament-scale analysis, introduce a fine lengthscale local to the turning point (take $x_T > 0$)

$$\bar{x} \sim \gamma (x - x_T) \tag{39}$$

where again $\gamma(k)$ is determined by asymptotic balance. In this stretched variable, the following perturbation expansions are used

$$f \sim s(\gamma)\, \bar{f}(\bar{x}),$$
$$r \sim R_T + \frac{1}{\gamma} R_T' \bar{x} + \bar{r}(\bar{x}) \tag{40}$$

where the scale factor $s(\gamma)$ is to be determined. Anticipating that the correction $\bar{r}$ is smaller than the first two Taylor terms of r, the rescaled $\bar{f}$ satisfies the Airy equation

$$\bar{f}'' - \frac{k^2}{\gamma^3} (\alpha |R_T'| \sin 2R_T)\, \bar{x} f = 0 \tag{41}$$

so that $\bar{f} = \mathrm{Ai}(\bar{x})$ on a caustic scale defined by

$$\gamma \sim (k^2 \alpha |R_T'| \sin 2R_T)^{1/3}. \tag{42}$$

Finally, as a verification of consistency, the scales

$$s(\gamma) = O\left(k^{1/6}\right), \quad \bar{r} = O\left(\frac{1}{k}\right) \tag{43}$$

are obtained by matching to the solutions from the oscillatory region.

The lengthscales for both the simple filaments and these special caustic solutions at the turning point are thus shown to both have the same $k^{-2/3}$-scaling property. This similarity of scaling supports the numerical observation that the filament structures in the optical/nematic experiments originate from focussing caustics. Observe the scaling similarity between the largest caustic peak and the single filament in Fig. 11. Also note the caustic-like resemblance in the $z = 2.0$ line plot of Fig. 3.

The numerical solutions of Fig. 11 were obtained by a numerical shooting method. Parameters for the filament were $\alpha = 0.25$, $|F_0|^2 \approx 79.4$, $R_0 = 1.1$ and $k \approx 1188.3$ for which the eigenvalue $\mu \approx 0.098$ was obtained. Parameters for the caustic were $\alpha = 0.25$, $|F_0|^2 \approx 7.26$, $R_0 = 1.1$ and $k \approx 1077.8$ for which the eigenvalue $\mu \approx 0.084$ was obtained. As a technical note, since both f and r must vanish at $x = \pm 1$ one might expect a two-parameter shoot, however this can be avoided by shooting in the eigenvalue μ on the decay of f and renormalizing the domain size as defined by the zero-crossings of $r(x)$ to the interval $[-1, 1]$.

7. Closing remarks

Within the context of a simple PDE model incorporating diffraction, refraction and nematic distortion, these computations clearly reproduce the self-focussing, undulation and filamentation phenomena as seen in the optical experiments and substantiated by asymptotic analysis. In our simulation of the experimental configuration, the numerics qualitatively reproduce the development of optical structure following the Frederiks transition of focal spots to filament pairs. These results also suggest how the undulation and filamentation of the quasi-steady asymptotic theory naturally arise from an initial value problem that more closely reflects the experimental situation.

While the paraxial PDE system (15),(16) models the physics of the self-focussing process in a nematic liquid crystal, it also bears considerable similarity to the nonlinear optics of thermal self-focussing. Since the nematic equation is in effect a time-independent nonlinear heat equation with a steady source term, it is not implausible that these results are related to the filamentation that has been observed in other nonlinear optical media [12,13].

The major simplifications inherent in the paraxial PDE model studied here are the reduction to two-dimensions, the omission of birefringence and polarization influences, and the neglect of scattering and absorption losses. Of these, the most restrictive assumption, in terms of phenomenology, seems to be the reduction of dimensionality. While the quantitative effects of the latter two are certainly important, their impact in the behavior of the PDE model seem qualitatively of lesser significance. The greatest obstacle to obtaining more quantitative comparison between experiment and the mathematics is that the cross-sectional intensity in two-dimensions has the wrong units. This is essentially because the independence in the y-coordinate is equivalent to a sheet of laser light (having infinite power) rather than a beam having finite cross-sectional area.

Analysis of a full-dimensional model which replaces the second derivative in x by an x-y Laplacian might possibly address two unresolved issues. The first is the discrepancy in the undulation wavelength from theory and computation ($\sim$ 15–20) to that observed in the experiment ($\sim$ 1–4). Re-establishing the correct dimensionality is likely to affect this wavelength since, from a Lagrangian perspective [6,9], there will be a proper scaling of the bulk light energy to the boundary energy of nematic. The second is the difference in the typical transverse profiles (Fig. 3) with two maxima from the distinct formation of filaments as interpreted from the experimental photographs. A possible resolution of this issue lies in a conjecture that the tendency to form distinct filaments is more prevalent in three dimensions. A derivation of scalings for an optical free-boundary asymptotics that includes the additional transverse y-dimension is under consideration.

Acknowledgements

The authors would like to thank Erez Braun, Luc Faucheux and Albert Libchaber for many enjoyable hours of scientific discussion regarding the optical experiments. The authors would like to also thank a referee for carefully reading the manuscript, and for making several useful comments. Both DJM and DWM were supported in part through AFOSR-90-0161 and NSF DMS-8922717 A01. DJM and MJS acknowledge partial support from DOE grant DE-FG02-88ER25053. MJS acknowledges the National Science Foundation through Presidential Young Investigator grant DMS-9396403. MJS also thanks Daniel Marcus for useful conversations. XPW is supported through the Research Grant Council of Hong Kong by grant D4053 DAG 93/94 sc14. The majority of the computations were performed using facilities at Illinois National Center for Supercomputing Application under grant DMS-94000N.

References

[1] Y.R. Shen, The Principles of Nonlinear Optics (Wiley, 1984).
[2] P.G. deGennes, The Physics of Liquid Crystals (Clarendon Press, Oxford, 1975).
[3] I.C. Khoo and Y.R. Shen, Liquid crystals: nonlinear optical properties and processes, Opt. Eng. 24 (1985) 579.

[4] E. Braun, L. Faucheux and A. Libchaber, Strong self-focusing in nematic liquid crystals, Phys. Rev. A 48 (1993) 1.
[5] E. Braun, L. Faucheux, A. Libchaber, D.W. McLaughlin, D.J. Muraki and M.J. Shelley, Undulation and filamentation in nematic liquid crystals, Europhys. Lett. 23 (1993) 4.
[6] D.W. McLaughlin, D.J. Muraki and M.J. Shelley, A paraxial theory for nonlinear optics in a nematic liquid crystal, in preparation (1994).
[7] D.W. McLaughlin, D.J. Muraki and M.J. Shelley, Physica D 68 (1993).
[8] D.W. McLaughlin, D.J. Muraki and M.J. Shelley, Self-focussed optical structures in a nematic liquid crystal, preprint (1994).
[9] N.V. Tabiryan, A.V. Sukhov and B.Ya. Zeldovich, The orientational optical nonlinearity of liquid crystals, Mol. Cryst. Liq. Cryst. (1986).
[10] A. Newell and J. Moloney, Nonlinear Optics (Addison-Wesley, 1990).
[11] G.H. Golub and C.F. Van Loan, Matrix Computations (Johns Hopkins University Press, 1983).
[12] F.W. Dabby and J.R. Whinnery, Thermal self-focusing of laser beams in lead glasses, Appl. Phys. Lett. 13 (1968) 284.
[13] A. Ashkin, J.M. Dziedzic and P.W. Smith, Continuous-wave self-focusing and self-trapping of light in artificial Kerr media, Opt. Lett. 7 (1982) 276.